Department of Physics
Faculty of Science

The Study of Spoof Surface Plasmon–Polartions (SSPPs) on a Hybrid Waveguide in Microwave Frequencies

written by
Tham Yap Fung

supervised by
Professor Ong Chong Kim

A thesis submitted in partial fulfillment of the requirements for the degree of Bachelor of Science with Honours
2014/2015

Abstract

Ever since the discovery of surface plasmons in 1950s [21], surface plasmon–polaritons (SPPs), among many other applications [5], has been prophesied to accelerate the development of new generation of photonic circuitry due to its subwavelength confinement ability [29]. While SSPs occurs naturally in optical frequencies, spoof surface plasmon–polaritons (SSPPs) which have similar characteristics as SPPs were proven to exist in lower frequencies such as terahertz and microwave frequencies on a plasmonic metamaterial [15]. Recently, the conversion of guided waves along a transmission line to SSPPs on plasmonic waveguide has been proposed by means of a hybrid waveguide [11]. In this project, the aforementioned conversion was first examined and verified via simulations. In addition, the behaviour of the SSPPs on the hybrid waveguide was investigated, and was found to be dependent on the physical parameters of the hybrid waveguide. On top of that, ring resonators were also incorporated to the hybrid waveguide, whose spectral response was then studied. The convenient manipulation of the SSPPs, together with the easy modification of the response of the hybrid waveguide by means of ring resonators, indicate great potentials for SSPPs devices to complement the existing techonology in microwave frequencies.

Acknowledgement

First and foremost, I would like to express my heartfelt gratitude to my supervisor, Prof Ong Chong Kim for his generosity in giving me the opportunity to work on my honours year project under his supervision. Over the course of the project, he has given me plenty of room and freedom, yet providing me guidance and support from time to time.

On top of that, I would also like to thank Mr Gong Chengsheng, a first year PhD student who came to Singapore under an exchange programme, which had given both of us a platform to learn from each other in the few months when he was here. His assistance has undoubtedly helped in my research in many ways.

Many thanks also to my coursemates who have accompanied me for the years in the university. We have been striving hard together to endure the challenges facing us. It is through the support and sharing among us that we continue to survive the hardship.

Last but not least, I am always indebted to the two most important persons in my life thus far, my parents. I would not be who I am today without their unconditional love ever since I was born. The immense care and selfless support that they have given is so much that I could hardly repay.

Contents

Chapter 1

Introduction

1.1 Background

The success in bringing optical fibers to practical use by Charles K. Kao has enabled the transmission of large amounts of information in the form of light around the globe in the modern world today [1]. The triumph in the fiber-optic communications has led to some part of the scientific community to postulate the replacement of electronics circuits with photonic devices [5]. Such a prophecy is further evidenced by the quantum limit to the Moore's Law that predicts the doubling of transistor density every two years. The quantum limit which argues that the Heisenberg uncertainty would ultimately limit the miniaturization of the electronic circuitry [17]. This, together with other challenges such as thermal dissipation, leakage current, and thermal noise further encourages the replacement of electric circuitry by photonic circitry.

However, the conventional photonic circuitry is bound to be limited by the diffraction limit, which requires the optical waveguide carrying the signals must be of a width at least half of the wavelength of the light travelling in it [5]. Such a limitation is undoubtedly an obstacle to the miniaturization of the circuitry and devices. The solution to a compact photonic integrated circuit beyond the diffraction limit lies in the surface–plasmon polaritons (SPPs) [25], which are "electromagnetic excitations propagating at the interface between a dielectric and a conductor, evanescently confined in the perpendicular direction" [13] to the propagation direction. Since the SPPs are confined at the metal–dielectric interface, subwavelength design of circuitry could therefore be realized.

While SPPs are found in infrared and optical frequencies, they do not exist naturally in lower frequency range such as the microwave frequencies. Nonetheless, surface waves known as spoof surface plasmon–polaritons (SSPPs) are supported by means of plasmonic metamaterial [15]. Hence, the advantages and benefits of SSPs can also be realized in the lower frequency regime with SSPPs, which have similar characteristics as SPPs in the counterpart of higher frequencies.

1.2 Motivation

As discussed in the previous section, SPPs and SSPPs have opened up a new avenue in the conveyance of signals from one point to another in a circuitry. The study of the properties of SSPPs such as their dispersion relation and their relationship with the behavior of a hybrid waveguide which supports SSPPs mode as well as the dependence of the properties of SSPPs on the physical characteristics of the hybrid waveguide in this project would definitely help in further understanding the nature of SSPPs.

In this project, the frequency band of interest lies within the microwave domain. Microwave technology have many niche applications in the military, commercial and scientific activities, such as the radar system for locating targets such as missile, motion sensor in automatic doors or security alarms in premises, and microwave radiometry for remote sensing of the earth and atmosphere [18]. By the scale invariance of classical electrodynamics, examining SSPPs in microwave frequencies in this project allows us to understand SSPPs in terahertz frequencies as well, since SSPPs are also supported at terahertz frequencies, which are given increasing attention recently as terahertz technology is believed to have a good prospect in many applications [27].

In the networked society today, signals take several forms in the course of their transmission. For an instance, signals might first be generated as electric signals in an electronic circuit, which are then converted to guided waves in transmission lines before transmitted as free propagating electromagnetic waves by an emitter, subsequently being captured by a receiver as guided waves, which

may then be transformed to SSPPs if necessary, as summarized in Figure 1.1. This project also studies the conversion of signals from the form of guided waves to SSPPs in a hybrid waveguide. The conversion of this kind is of particular importance because the devices and instrument used in the microwave frequency bands often distribute the signals and energies in the form of guided waves along transmission lines. Thus, the conversion from guided waves to SSPPs and vice versa would allow greater integration of SSPPs in the conventional microwave circuitry.

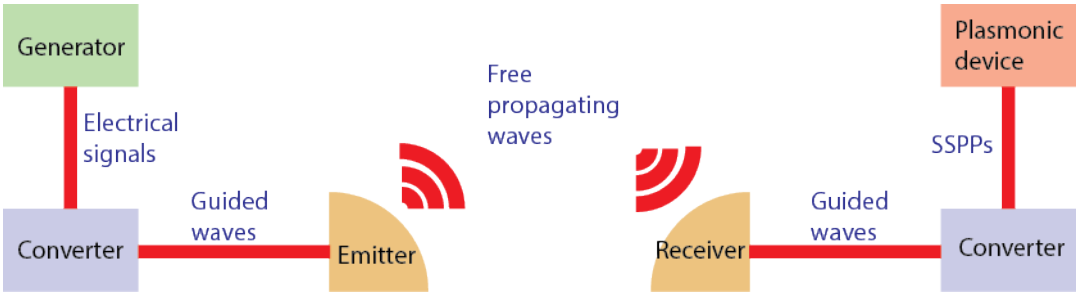

Figure 1.1: Conversion of signals during transmission.

In addition, this project also aims to evaluate the practicality and functionality of the hybrid waveguide by examining the behaviour of SSPPs with respect to the change of physical properties of the waveguide. The incorporation of ring resonators to the hybrid waveguide also explores the likelihood of such a plasmonic device to replace or complement traditional microwave devices.

Chapter 2

Fundamentals

2.1 Spoof Surface Plasmon–Polaritons (SSPPs)

As the name suggests, spoof surface plasmon–polartions (SSPPs), also known as designer surface plasmon–polaritons, are a form of electromagnetic surface waves which, to a certain extent, share similar behaviour with surface plasmon–polartions (SPPs). Hence, it would be appropriate to examine some basic properties of SPPs before looking at the proof that SSPPs indeed mimic SPPs.

As mentioned, SPPs are a form electromagnetic excitation whose amplitude decays exponentially into the mediums between which the interface at which SPPs exist. SPPs are a product of the coupling between electromagnetic waves in the dielectric medium and the plasma oscillations in the metal, as summarized in Figure 2.1.

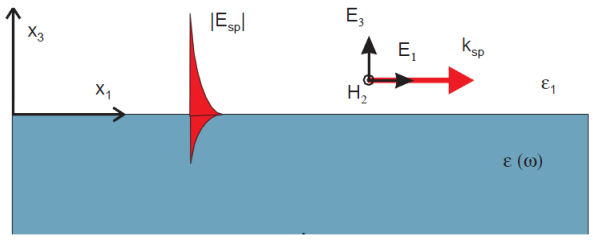

Figure 2.1: SPPs at metal–dielectric interface [29].

The boundary conditions of the solutions of Maxwell equations at the interface of the two mediums require one of the mediums to have a negative dielectric permittivity [29]. The demand for a medium to have a negative permittivity is

fulfilled as the dielectric function of a metal is given by [7]

$$\epsilon(\omega) = \epsilon(\infty)\left(1 - \frac{\omega_p}{\omega}\right) \tag{2.1}$$

where $\epsilon(\infty)$ is a constant due to the positive ions background and ω_p is the plasma frequency. It can be seen that when the frequency of the electromagnetic waves, ω is smaller than the plasma frequency, ω_p, the resulting dielectric function, $\epsilon(\omega)$ of the metal will be negative and hence SPPs could be supported at these frequencies.

The dispersion relation of SPPs is given as follows [29].

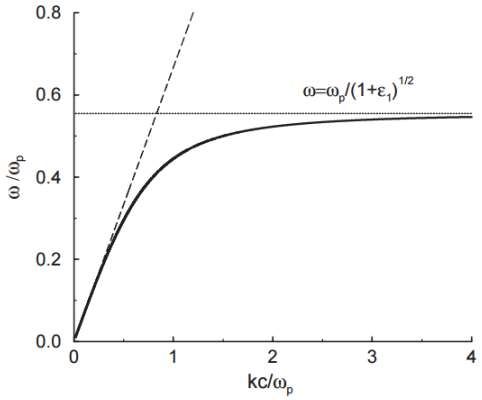

Figure 2.2: Dispersion relation of SPPs [29].

While SPPs are found in infrared and optical frequencies, they do not exist naturally in lower frequency range, in which the metal behaves as a perfect electric conductor (PEC) [12]. Hence, the SPPs are generally not found in far-infrared, terahertz and microwave frequencies [22]. This is due to the fact that metals in far infrared, terahertz and microwave frequencies have their dielectric response to be dominated by the large imaginary component corresponding the high conductivity [10, 12]. Since electric field vanishes inside the metal, plasma oscillations and SSPs could not be supported.

In the year 2004, Pendry et al. proved that SPPs-like modes called spoof surface plasmon–polaritons (SSPPs) could be supported in the lower frequency bands [15]. They established a close relationship between SPPs and SSPPs, having proven that SSPPs are governed by a dielectric function similar to that of a metal where SPPs are present. SSPPs are made possible with plasmonic

matematerials which can be created by introducing periodic defects or structures on metallic surfaces, such as a perforated metallic surface as shown in Figure 2.3.

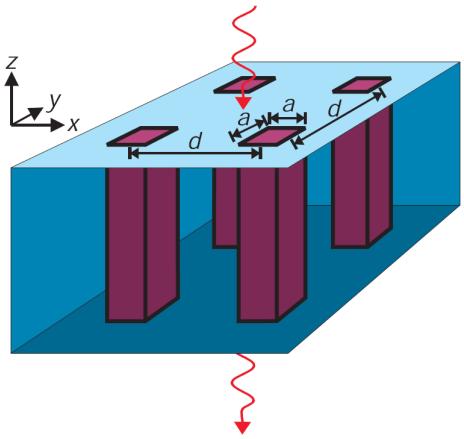

Figure 2.3: Perforated metallic surface which supports SSPPs [15] with holes of dimensions of a and a period of d.

Besides holes, other periodic structures such as arrays of blocks or grooves in which bound states of electromagnetic fields can exist are also capable of supporting SSPPs [15].

Several waveguide modes especially the fundamental mode which decays the least will be induced in the holes upon being impinged by an incident waves. As $a < d << \lambda_0$ where λ_0 is the wavelength of the incident waves in free space, the incident waves are insensitive to the details of the surface and the perforated surface is regarded to have an effective response of ϵ_x and ϵ_y, where ϵ stands for the dielectric function. By equating the instantaneous energy flow inside and outside the surface and after some mathematical manipulations and assumptions, the dielectric function of the surface is effectively given by

$$\epsilon_x = \epsilon_y = \frac{\pi^2 d^2 \epsilon_h}{8a^2}\left(1 - \frac{\pi^2 c^2}{a^2\omega^2\epsilon_h\mu_h}\right) \tag{2.2}$$

where ϵ_h and μ_h are the respective relative permittivity and relative permeability of materials inside the holes while c is the speed of light in vacuum. Equation 2.2 can be further reduced to

$$\epsilon_x = \epsilon_y = \frac{\pi^2 d^2 \epsilon_h}{8a^2}\left(1 - \frac{\omega_p^2}{a^2\omega^2}\right) \tag{2.3}$$

where $\omega_p = \dfrac{\pi c}{a\sqrt{\epsilon_h \mu_h}}$.

Pendry et al. further state that the dispersion relation of the SSPPs are given by

$$k_{||} = \frac{1}{c}\sqrt{\omega^2 + \frac{1}{\omega_p^2 - \omega^2}\frac{64a^4\omega^2}{\pi^4 d^4}} \tag{2.4}$$

where $k_{||}$ is the wavenumber of the SSPPs along the interface.

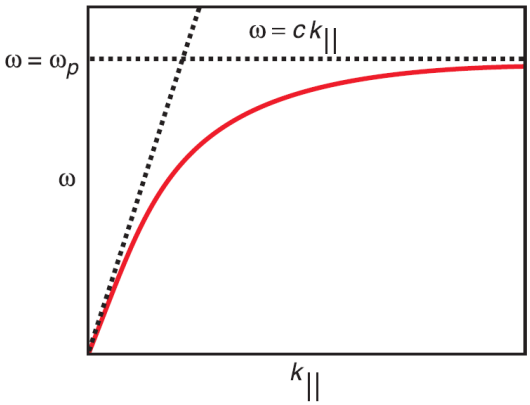

Figure 2.4: Dispersion relation of SSPPs [15].

Examining the effective dielectric functions, Equation 2.1 and Equation 2.2, and the dispersion relations, Figure 2.2 and Figure 2.1, of SPPs and SSPPs would lead to a conclusion that both SPPs and SSPPs behave in a similar manner even though their origins are not exactly the same.

2.2 Transmission Line Theory

While an electronic circuit is treated with the lumped element model, in which the current and voltage are assumed to have no significant change over the circuit, a transmission line is a distributed parameter network over which the current and voltage change in magnitude and phase [18]. A transmission line is often denoted with two-wire lines as shown in Figure 2.5.

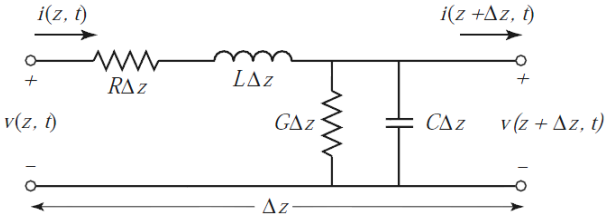

Figure 2.5: Schematic diagram of a transmission line [18].

where R, L, G and C are the series resistance per unit length for both conductors, series inductance per unit length for both conductors, shunt conductance per unit length and shunt capacitance per unit length. Using Kirchhoff's Voltage Rule and Kirchhoff's Current Rule, under sinusoidal steady state condition, we have [18]

$$\frac{d^2V}{dz^2} - \gamma^2 V = 0 \tag{2.5}$$

$$\frac{d^2I}{dz^2} - \gamma^2 I = 0 \tag{2.6}$$

where $\gamma = \alpha + j\beta = \sqrt{(R + j\omega L)(G + j\omega C)}$ and ω is the angular frequency. In the case of a lossless transmission line, γ is reduced to $\gamma = j\beta = \omega\sqrt{LC}$.

An important property of a transmission line is its characteristic impedance, Z_0. It is the ratio of the complex voltage to the complex current along the transmission line. The characteristic impedance of a transmission line modeled as in Figure 2.5 is given by [18]

$$Z_0 = \sqrt{\frac{R + j\omega L}{G + j\omega C}} \tag{2.7}$$

which is simplified to the following for a lossless transmission line.

$$Z_0 = \sqrt{\frac{L}{C}} \tag{2.8}$$

Transmission lines such as coaxial cables, and connectors typically have a characteristic impedance Z_0 of 50 Ω. This is because maximum power capacity and minimum attenuation occur at 30 Ω and 77 Ω respectively. Thus 50 Ω is a compromise of the two desired features of a transmission line [18].

There are many types of transmission lines, these include coaxial cable, stipline, microstrip and coplanar waveguide (CPW). Examples of the field distribution in these transmission lines is show in Figure 2.6.

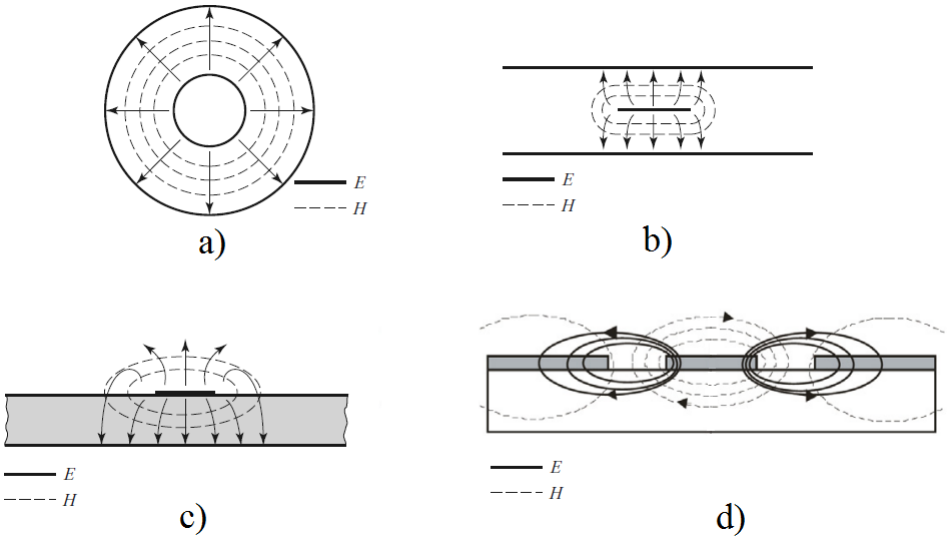

Figure 2.6: Examples of field distribution in a) coaxial cable, b) stripline, c) microstrip, and d) coplanar waveguide (CPW) [16, 18].

Chapter 3

Methodology

In this project, computer simulation is adopted as the main approach in investigating a hybrid waveguide and modeling the properties of SSPPs on the hybrid waveguide. Two commercial simulation software programmes – ANSYS High Frequency Structural Simulator (HFSS) and CST Microwave Studio (MWS) were used in the course of the project. Other software such as MATLAB was also used for some calculations required in designing the hybrid waveguide.

3.1 ANSYS High Frequency Structural Simulator (HFSS) [4]

HFSS is a 3D full wave electromagnetic simulator mainly used in the design and simulation of circuit components, antenna, etc. in the radiowave and microwave frequencies. The HFSS solver uses a numerical method called finite element method (FEM) which divide the volume in analysis into many subdomains which are collectively known as a mesh, and subsequently solve the problem in each of the subdomain.

HFSS solves for the electric field subject to the boundary conditions and excitations for each finite element or subdomain and solves for the magnetic field from the calculated electric field.

$$\nabla \times \left(\frac{1}{\mu_r} \nabla \times \vec{E} \right) - k_0^2 \epsilon_r \vec{E} = 0 \tag{3.1}$$

$$\vec{H} = \frac{j}{\omega\mu}\nabla \times \vec{E} \tag{3.2}$$

In order to ensure the solution obtained is accurate, HFSS uses an adaptive analysis process which deliberately changes the mesh until the right solution is found. The process is summarized in Figure 3.1

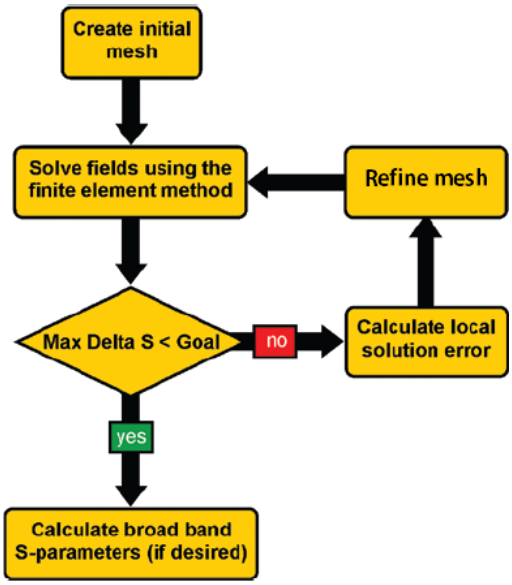

Figure 3.1: Adaptive analysis in HFSS [4].

An initial mesh is firstly generated and the electric fields are approximated as $\vec{E}_{approx}$ at a solution frequency. The approximated fields $\vec{E}_{approx}$ are then substituted to Equation 3.3 to calculate the degree of error or residue.

$$\nabla \times \left(\frac{1}{\mu_r}\nabla \times \vec{E}_{approx}\right) - k_0^2\epsilon_r\vec{E}_{approx} = residue \tag{3.3}$$

Then, a predefined fraction of the finite elements in the regions with large residue is refined by replacing the large tetrahedral elements with the smaller ones. The process of solving, residue analysing, and remeshing are repeated iteratively until the convergence criteria or the maximum number of iterative passes are fulfilled. If the analysis is to be carried out with a frequency sweep, the last refined mesh at the solution frequency will be used for other frequencies.

3.2 CST Microwave Studio (MWS)

CST MWS, a module of CST Studio Suite, is a 3D electromagnetic simulation software for high frequency components. It offers a wide range of solvers which operate in both time domain and frequency domain [2] and is also based on the finite element method (FEM). Among the solvers available include transient solver, frequency domain solver, eigenmode solver, integral equation solver, asymptotic solver and TLM solver.

In the aspects of speed and memory requirement, the transient solver in CST MWS has an edge over HFSS. This is because the transient solver is a time domain solver which runs the calculation once by supplying an input signal or pulse to the model in study. It then calculates the resulting field distribution in the model and the mode amplitudes in other ports of the model. The results are then processed to give the S parameters of the model at every frequency by means of Fourier transform [2]. On the other hand, HFSS which uses frequency domain solver in calculating the S parameters performs the calculation at every frequency in the range and hence demands substantially large amount of memory and takes very long time for a single simulation. However, it was found that the simulation results calculated CST MWS could be very inaccurate sometimes when a simulation was not carefully set up. Therefore, a major part of simulations in this project were still carried out using HFSS.

3.3 Simulation Setup

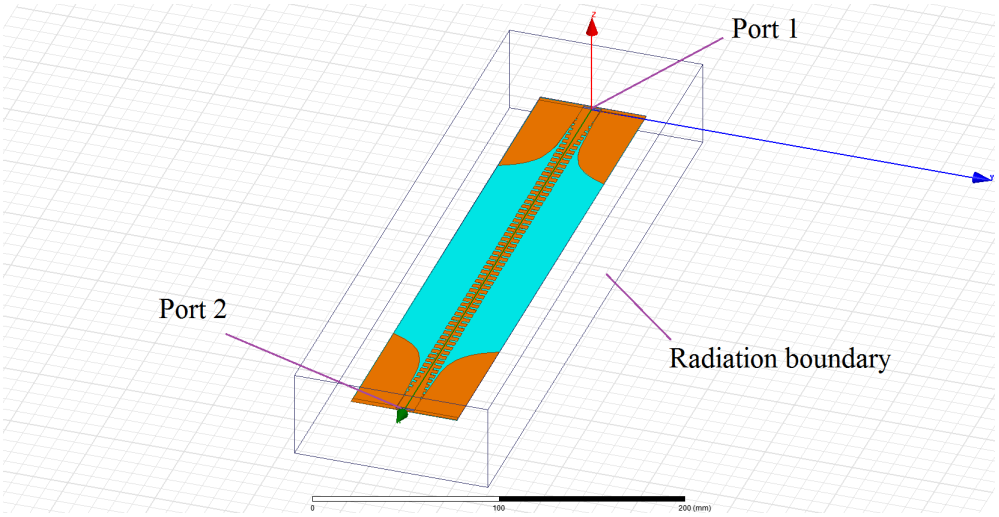

Figure 3.2: Model built in HFSS.

In this project, a 3D model of a hybrid waveguide with desired dimensions and materials was first built in HFSS. Next, a vacuum box with radiation outer boundary was created around the waveguide. Excitations were then assigned in the form of two lumped ports at the two ends of the hybrid waveguide. In the solution setup, the maximum number of adaptive passes was increased to 12 so as to obtain an accurate solution. The frequency sweep was set from 0.1 GHz to 14.0 GHz, 15.0 GHz or 16.0 GHz with a step size of 0.1 GHz or 0.2 GHz depending on the needs. Next, the built model was analyzed and a single simulation typically took at least 3 days to complete. Finally, the results were post processed by plotting the scattering parameters and field distribution over the frequency range. The entire process of the simulation is summarized in Figure 3.3 as follows.

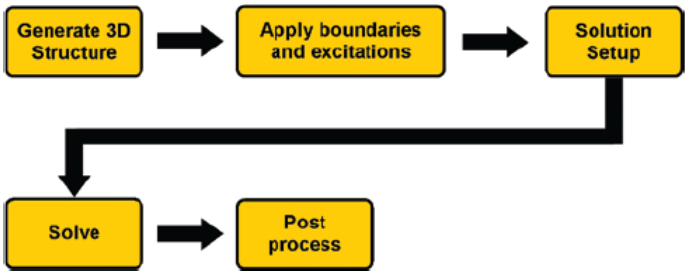

Figure 3.3: Flow chart of a typical simulation in HFSS [4].

On the other hand, the eigenmode solver of CST MWS was used in the calculation of the dispersion relation of the SSPPs on the hybrid waveguide. A unit cell of the plasmonic waveguide was first constructed, with appropriate boundary conditions assigned on the unit cell, as shown in Figure 3.4, where periodic boundary conditions were applied along the positive and negative x directions.

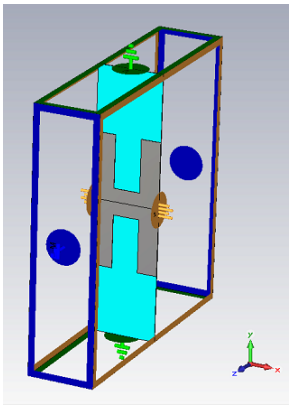

Figure 3.4: A unit cell for eigenmode analysis in CST MWS.

By the periodicity of the hybrid waveguide, the independent values of the wavenumber, k_x of the SSPPs on the hybrid waveguide is given by

$$-\frac{\pi}{2} \leq k_x p \leq \frac{\pi}{2} \tag{3.4}$$

where p is the period of the structure. The quantity $k_x p$ was defined as a variable $phase\_x$, and was swept from 0° to 180° with a step size of 15° using the parameter sweep option in the eigenmode solver to obtain the dispersion graph, which is the relationship between frequency f and wavenumber k_x.

Chapter 4

Construction of a Hybrid Waveguide

Recently, H. F. Ma et al. have presented a hybrid waveguide which allows high efficiency broadband conversion of guided waves to SSPPs and vice versa [11]. The presented waveguide, as shown in Figure 4.1, is composed of three parts.

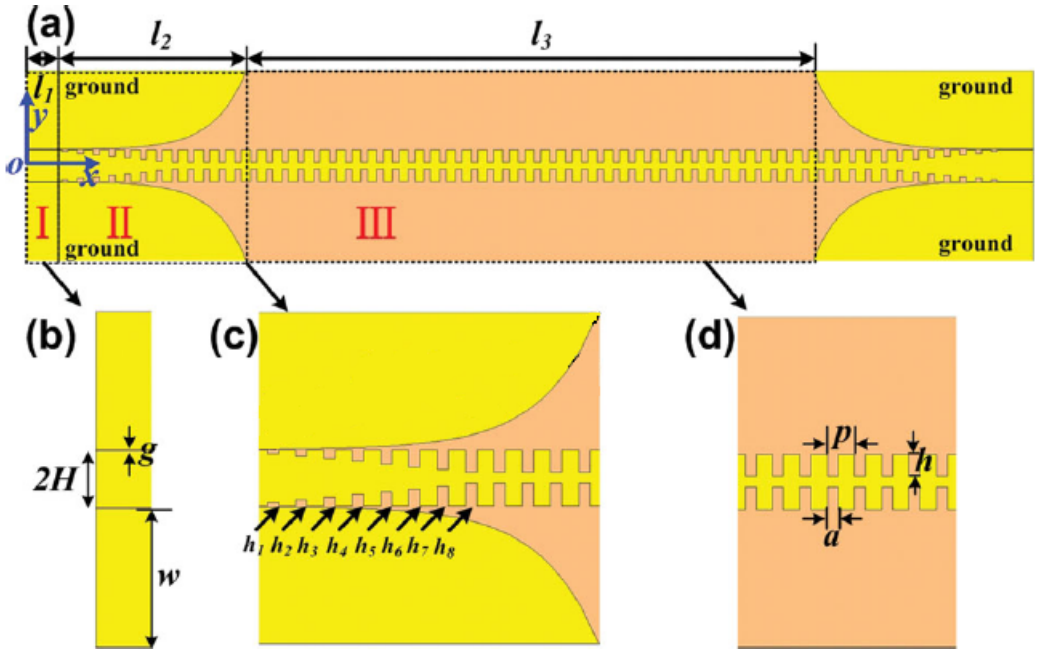

Figure 4.1: Geometry of the hybrid waveguide [11].

Part I is a conventional coplanar waveguide with a central strip of width $2H = 10\ mm$ and ground plates of width $w = 25\ mm$ each; Part III is a plasmonic waveguide which is essentially a corrugated metallic strip with rectangular

grooves of depth $h = 4\ mm$, width $a = 2\ mm$ and period $p = 5\ mm$ on the dielectric substrate; while Part II is a transition from Part I to Part III, in which the width of the ground plates are gradually decreased to zero and the central strip is corrugated with the groove depth increases from 0.5 mm to 4 mm at a step size of 0.5 mm. The copper plates and strip above the substrate has a thickness of $t = 0.018\ mm$ whereas the substrate is FR4-epoxy with a thickness of $d = 0.05\ mm$.

4.1 Dispersion Relation of SSPPs

The behaviour of SSPPs on each side of the thin corrugated metallic strip can be approximately modeled as that on a infinitely thick (in y direction) corrugated metal as shown in Figure 4.2. In so doing, the complications arising from the thinness of the strip can be avoided and the analysis is made simpler. The period and the depth of the periodic grooves are labeled as p and h respectively and the medium above the metal is having an isotropic relative permittivity of ϵ_r.

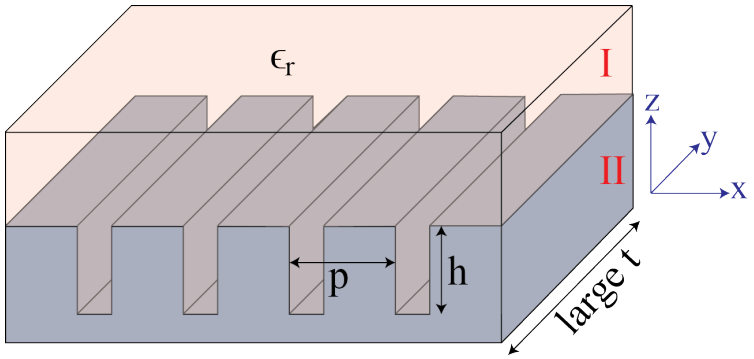

Figure 4.2: Corrugated metal with infinitely large thickness.

In deriving the dispersion relation [24], the magnetic field of the TM waves in region I could be expressed as Floquet modes for periodic structures,

$$H_y^I = \sum_{n=-\infty}^{\infty} \rho_n \exp(-jk_{x,I}^{(n)}x) \exp(-jk_{z,I}^{(n)}z) \tag{4.1}$$

where ρ_n is the diffraction amplitude,

$$k_{x,I}^{(n)} = k_x + 2\pi n/p \tag{4.2}$$

and

$$(k_{x,I}^{(n)}/\sqrt{\epsilon_r})^2 + (k_{z,I}^{(n)}/\sqrt{\epsilon_r})^2 = (\omega/c)^2 \tag{4.3}$$

In region II, the magnetic field is only non-zero in the grooves. The magnetic field in region II is expressed as follows.

$$H_y^{II} = A^+ \exp(jk_{z,II}z) + A^- \exp(-jk_{z,II}z) \tag{4.4}$$

where A^+ and A^- are constants and

$$k_{z,II} = \sqrt{\epsilon_r}\omega/c \tag{4.5}$$

Solving the boundary conditions between region I and region II, we have

$$\begin{pmatrix} \sum \frac{S_n^2 k_{z,II}}{k_{z,I}^{(n)}} - 1 & -\sum \frac{S_n^2 k_{z,II}}{k_{z,I}^{(n)}} - 1 \\ \exp(jk_{z,II}h) & -\exp(jk_{z,II}h) \end{pmatrix} \begin{pmatrix} A^+ \\ A^- \end{pmatrix} = \begin{pmatrix} 0 \\ 0 \end{pmatrix} \tag{4.6}$$

which implies

$$1 - j\sum_n \left(\frac{k_{z,II} S_n^2}{k_{z,I}^{(n)}} \right) \tan(k_{z,II}h) = 0 \tag{4.7}$$

where

$$S_n = \sqrt{\frac{a}{p}} \text{sinc}\left(k_x^{(n)} \frac{a}{2}\right) \tag{4.8}$$

In the limit that $\lambda \gg d, h$ and $k_x a \ll 1$, the zeroth order S_0 dominates and $S_0 \approx \sqrt{\frac{a}{p}}$. Equation 4.7 becomes

$$k_x = \sqrt{\epsilon_r}\frac{\omega}{c}\sqrt{1 + \left(\frac{a}{p}\right)^2 \tan^2\left(h\sqrt{\epsilon_r}\frac{\omega}{c}\right)} \tag{4.9}$$

which is further reduced to

$$k_x = k_0\sqrt{1 + \left(\frac{a}{p}\right)^2 \tan^2\left(h\frac{\omega}{c}\right)} \tag{4.10}$$

when region I is a medium of air or vacuum with $\epsilon_r = 1$. From Equations 4.9 and 4.10, it is clear that the dispersion relation of the SSPPs are dependent on

the geometry and material property of the hybrid waveguide.

The Equations 4.9 and 4.10 refer to the case of an infinitely thick corrugated metal. The structure of the designed hybrid waveguide is however different as in Figure 4.3.

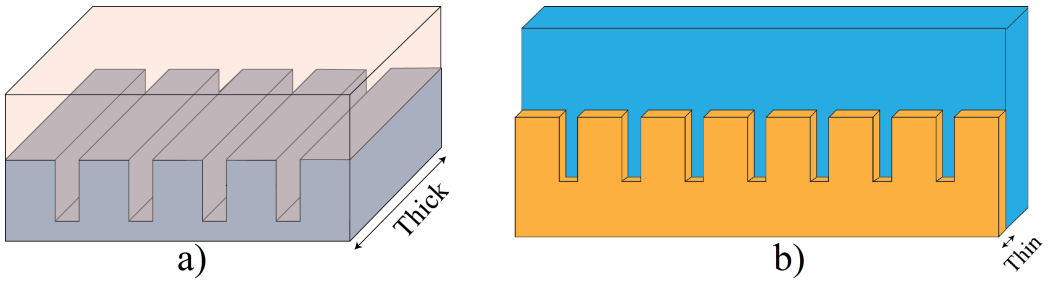

Figure 4.3: a) Model used in derivations; b) Structure of hybrid waveguide.

The actual dispersion relation of the SSPPs on the hybrid waveguide was obtained by running a simulation, as described in Section 3.2. The results are as follows.

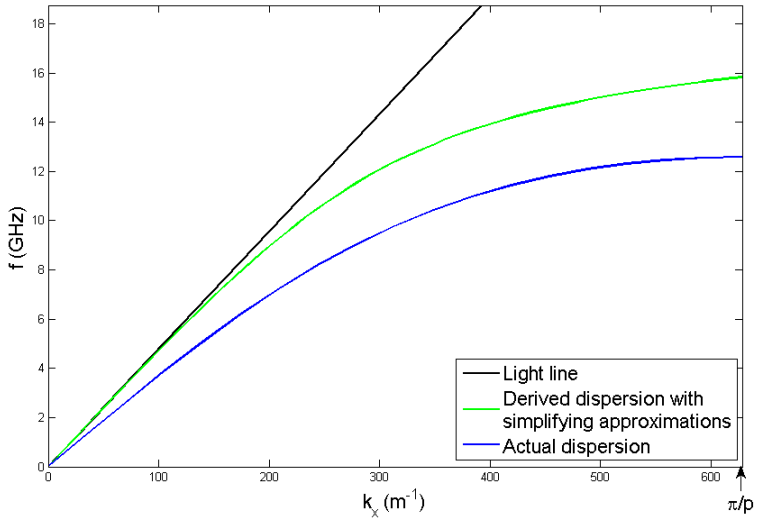

Figure 4.4: Light line and dispersion relations of SSPPs.

From the simulation, it can be seen that the dispersion relation of the SSPPs on the actual structure of the hybrid waveguide deviates even further from the light line compared to that of the model used in derivations.

4.2 Momentum and Impedance Matching

In designing the hybrid waveguide, two important concerns must be addressed so as to enable the conversion of the guided waves mode in a coplanar waveguide (CPW) to SSPPs mode in the corrugated metal strip. They are the momentum mismatch and the impedance mismatch between the guided waves and SSPPs.

As seen in the dispersion graph in Figure 4.4, the value of the wavenumber of SSPPs, k_x is always larger than that of the guided waves in the CPW, k_0 at any given frequency. Thus, there exist a large momentum mismatch between CPW in region I and the corrugated strip in region III of Figure 4.1. In order to solve the momentum mismatch, it is crucial to bridge the gap between the momenta of the two modes.

From Equation 4.10,

$$k_x = \frac{\omega}{c}\sqrt{1 + \left(\frac{a}{p}\right)^2 \tan^2\left(h\frac{\omega}{c}\right)} \tag{4.10}$$

it is clear that when k_x is closer to k_0 when h is smaller. Therefore, the metallic strip in Region II of Figure 4.5 is corrugated in a way that the depth of the grooves, h is increasing gradually from 0 mm to 4 mm with a step size of 0.5 mm so that the momentum mismatch can be reduced in each period, p at all frequencies.

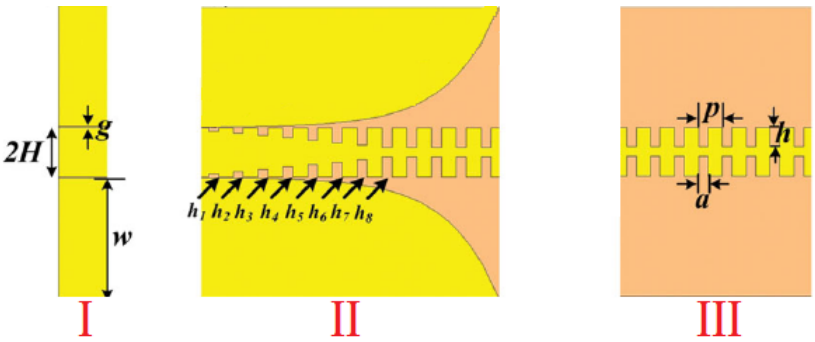

Figure 4.5: Regions I, II and III of the hybrid waveguide [11].

On the other hand, impedance matching is an important consideration in designing the waveguide. The reflection coefficient, Γ of a wave incident on a

medium with impedance Z_b from a medium with impedance Z_a is given by [18]

$$\Gamma = \frac{Z_b - Z_a}{Z_b + Z_a} \tag{4.11}$$

Hence, the difference in impedance of any two adjacent points along the waveguide must not be big so that the reflection at the interface is negligible. The characteristic impedance of a coplanar waveguide is dependent on the width of the central strip $2H$, the gap between the central strip and the ground plates g, the thickness of the ground plate and central strip and the dielectric constant of the dielectric substrate, ϵ_r.

Therefore, the change of the value of g from 0.244 mm in Region I to infinity in Region III would induce a large difference in the impedance and hence a large reflection. Therefore, the transition was designed in a way that the gap, g between the central strip and ground plates is increased gradually so that the impedance difference of any two adjacent planes along the hybrid waveguide is negligibly small and hence the signals and energies can be fed from the CPW in Region I to plasmonic corrugated strip in Region III without too much of reflection.

4.3 Simulation Results

Simulation on the hybrid waveguide was done to investigate its performance and efficiency in the conversion of guided waves to SSPPs and the propagation of SSPPs along the waveguide.

The plot of the magnitude of the electric field on the hybrid waveguide at a frequency of 10 GHz is shown in Figure 4.6. It is seen from Figure 4.6 that most of the energies are in fact confined near the metallic surface of the CPW as well as the corrugated strip. This is consistent with Pendry's prediction that metallic surfaces with periodic defects, such as the corrugated metallic strip in this case, do support SPPs-alike surface waves known as SSPPs.

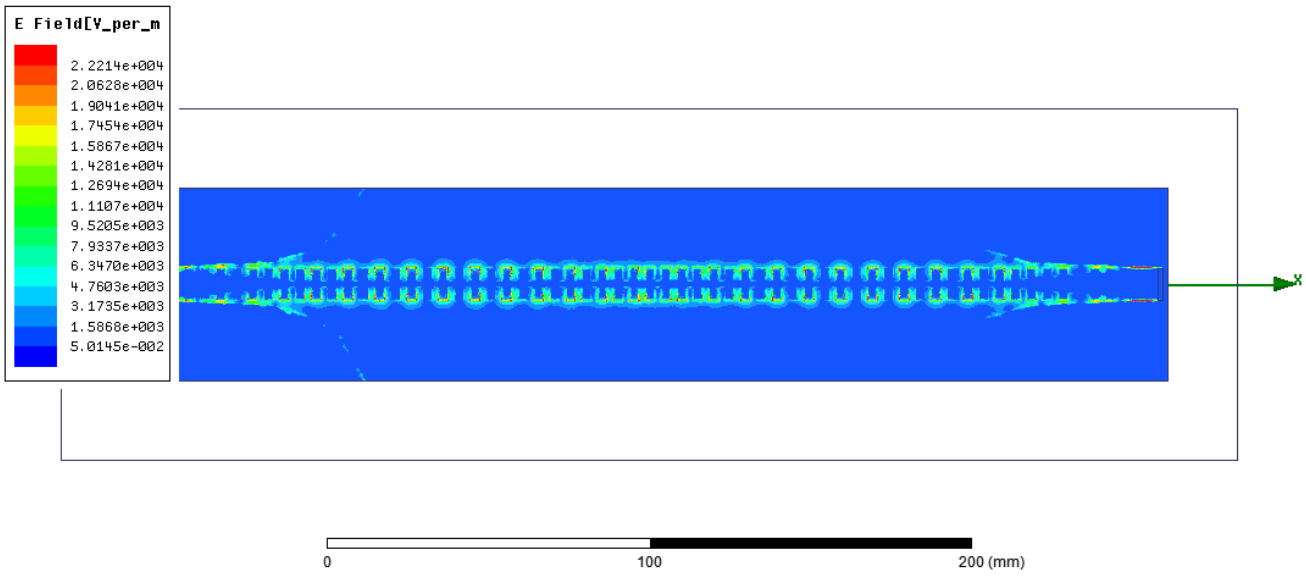

Figure 4.6: The magnitude of the electric field on the hybrid waveguide at a frequency of 10 GHz.

The efficiency of the conversion of guided waves to SSPPs and vice versa and that of the propagation of the SSPPs along the hybrid waveguide for the frequency range from 0.1 GHz to 14.0 GHz are given by the $S11$ and $S21$ parameters as follows.

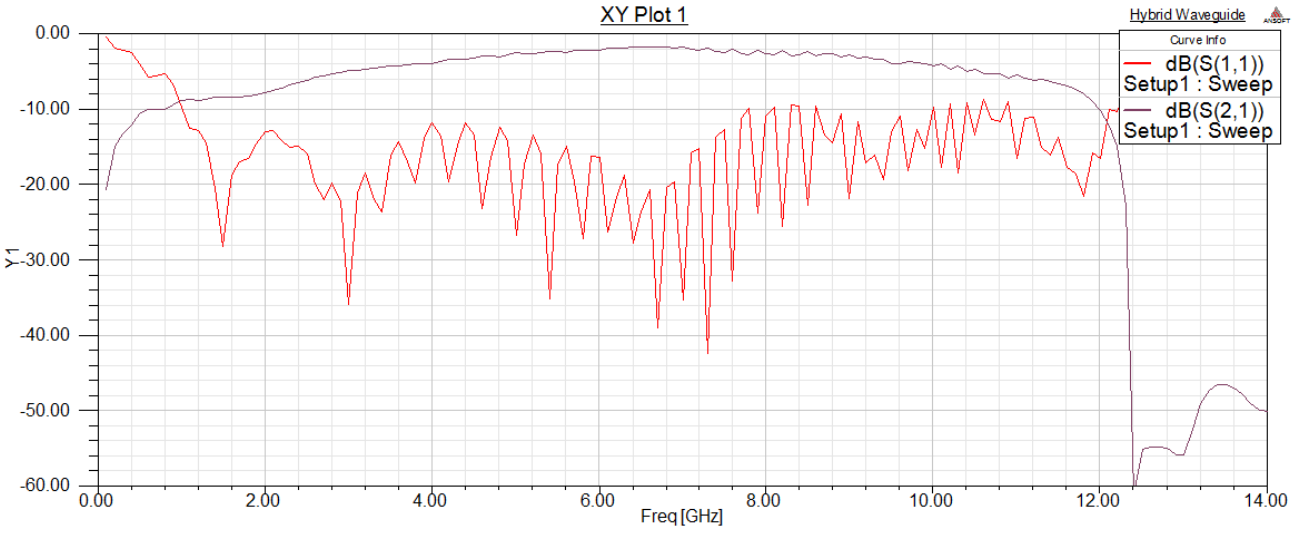

Figure 4.7: The magnitude of the electric field on the hybrid waveguide at a frequency of 10 GHz.

From the graph, the $S11$ parameter is low while the $S21$ parameter is high in the range from approximately 1.0 GHz to around 12.0 GHz. This implies that the reflection of signals is low whereas the transmission of energies from one end to another of the waveguide is high in this frequency range.

In fact, the hybrid waveguide acts as a bandpass filter which allows signals of a certain band of frequencies to transmit but reject signals of frequencies outside the band, at the same time allows the conversion between the guided waves mode in a conventional CPW and the SSPPs mode in a corrugated metallic strip. The conversion of such kind is highly important because it bridges the conventional transmission line technology to the newer science of plasmonic metamaterial.

Chapter 5

Manipulation of SSPPs on the Hybrid Waveguide

As seen in the previous section, the hybrid waveguide basically acts as a band-pass filter which allows signals within a certain range of frequency to transmit along it. In this chapter, it will be shown how the bandwidth of the transmission band could be altered, by simply varying the physical properties of the hybrid waveguide.

5.1 Upper Cutoff Frequency

In Section 4.1, it has been shown that the disperion relation of the SSPPs on the hybrid waveguide is approximated by Equation 4.9

$$k_x = \sqrt{\epsilon_r}\frac{\omega}{c}\sqrt{1+\left(\frac{a}{p}\right)^2 \tan^2\left(h\sqrt{\epsilon_r}\frac{\omega}{c}\right)} \tag{4.9}$$

Differentiating k_x with respect to ω, we have

$$\frac{dk_x}{d\omega} = \frac{\sqrt{\epsilon_r}}{c}\left(\frac{A^2+\omega\left(\frac{a}{p}\right)^2\sqrt{\epsilon_r}\frac{h}{c}\tan^2\left(\sqrt{\epsilon_r}\frac{h\omega}{c}\right)\sec^2\left(\sqrt{\epsilon_r}\frac{h\omega}{c}\right)}{A}\right) \tag{5.1}$$

where $A \equiv \sqrt{1 + \left(\frac{a}{p}\right)^2 \tan^2\left(h\frac{\omega}{c}\right)}$.

The group velocity, v_g of the SSPPs along the corrugated strip is given by $\frac{d\omega}{dk_x}$, which is the reciprocal of the expression in Equation 5.1. With that,

$$v_g = \frac{c}{\sqrt{\epsilon_r}} \left(\frac{A}{A^2 + \omega \left(\frac{a}{p}\right)^2 \sqrt{\epsilon_r}\frac{h}{c} \tan^2\left(\sqrt{\epsilon_r}\frac{h\omega}{c}\right) \sec^2\left(\sqrt{\epsilon_r}\frac{h\omega}{c}\right)} \right) \tag{5.2}$$

Denoted as f', the upper cutoff frequency of the bandwidth of the hybrid waveguide is the frequency at which no signal is able to propagate along the waveguide. In other words, at the upper cutoff frequency f' (corresponding to ω'), the group velocity v_g of the SSPPs is essentially zero.

$$v_g(\omega = \omega') = 0 \tag{5.3}$$

Therefore, from Equations 5.2 and 5.3, we have

$$A = 0 \tag{5.4}$$

$$\sqrt{1 + \left(\frac{a}{p}\right)^2 \tan^2\left(\sqrt{\epsilon_r}h\frac{\omega'}{c}\right)} = 0 \tag{5.5}$$

$$\tan\left(\sqrt{\epsilon_r}h\frac{\omega'}{c}\right) = i\frac{d}{a} \tag{5.6}$$

$$\omega' = \frac{c}{\sqrt{\epsilon_r}h}\frac{\pi}{2} \tag{5.7}$$

$$f' = \frac{c}{4\sqrt{\epsilon_r}h} \tag{5.8}$$

The expression of the upper cutoff frequency f' in Equation 5.8 shows that its value is dependent on the dielectric constant, ϵ_r' of the substrate and the groove depth, h of the corrugated metallic strip.

However, it should be noted that the dispersion relation in Equation 4.9 is derived based on an infinitely thick corrugated model but not a thin metallic strip on the top of a dielectric substrate, depicted in Figure 4.3. Therefore, the

expression in Equation 5.8 does not serve as an exact numerical solution for upper cutoff frequency in the hybrid waveguide, yet it gives the general trend of the upper cutoff frequency in response to the change of physical properties of the waveguide.

5.2 Varying Substrates

Equation 5.8 predicts that as the dielectric constant, ϵ_r of the substrate increases, the upper cutoff frequency, f' decreases and the bandwidth decreases. Three materials of different dielectric constant, ϵ_r were chosen in the simulations to verify the above mentioned relationship.

It should be taken note that the dielectric constant, ϵ_r of the substrate of a CPW is one of the determinants of its characteristic impedance, Z_0. Therefore, while substrates of different dielectric constants, ϵ_r are used, the gap between the central strip and the ground plates, g is adjusted accordingly so that the characteristic impedance, Z_0 of the CPW in the hybrid waveguide remains as 50 Ω. The MATLAB code for computing the characteristic impedance,Z_0 using the physical parameters of a CPW is included in Appendix A [6, 23] for reference.

The graphs of the S parameters for a frequency range from 0.1 GHz to 14.0 GHz of the hybrid waveguides of different substrates, namely Rogers RT/duriod 6002, FR4-epoxy and Rogers RT/duroid 6006 are shown in Figure 5.1, 5.2 and 5.3 respectively.

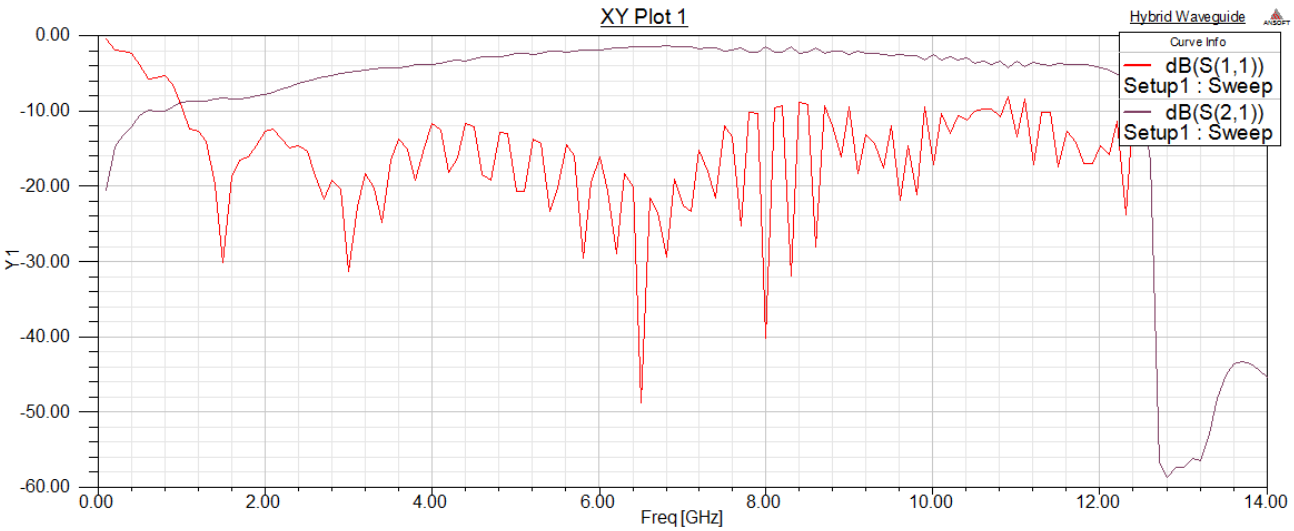

Figure 5.1: S parameters of the hybrid waveguide with a substrate of $\epsilon_r = 2.94$.

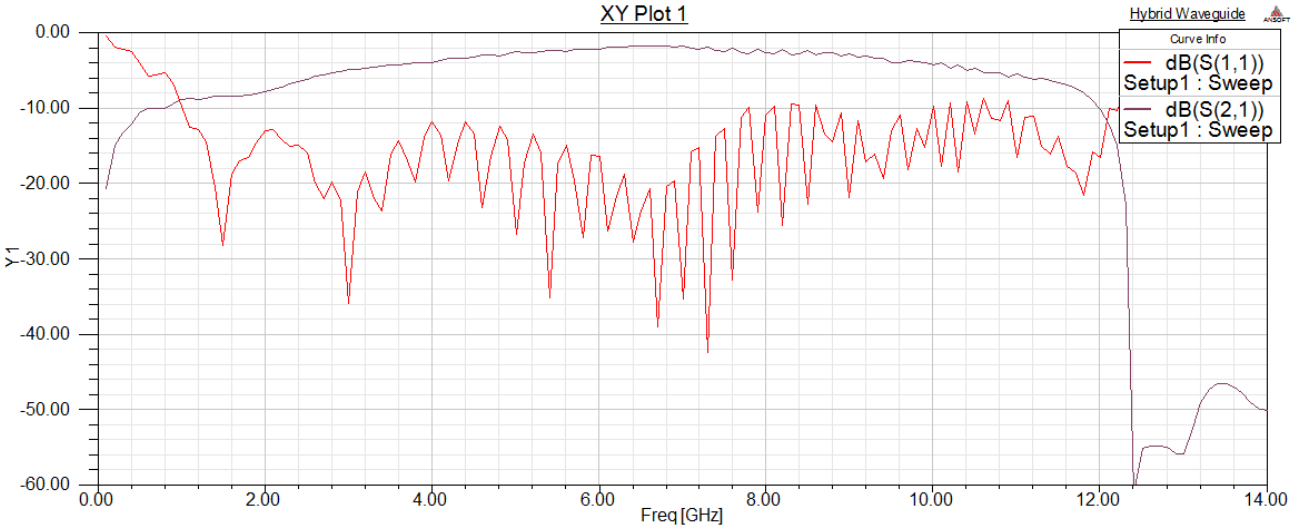

Figure 5.2: S parameters of the hybrid waveguide with a substrate of $\epsilon_r = 4.4$.

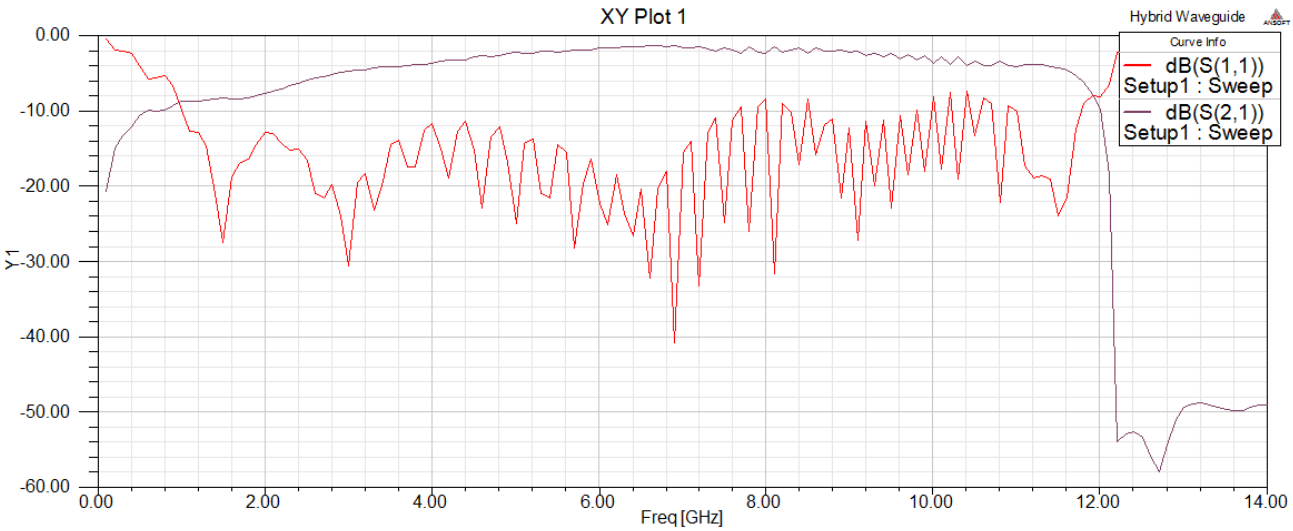

Figure 5.3: S parameters of the hybrid waveguide with a substrate of $\epsilon_r = 6.15$.

Choosing the cutoff frequency, f' to be first frequency at which the $S21$ parameter is lower than $-25\ dB$ in the vicinity of a large drop of the $S21$ parameter, the results are summarized in Table 5.1 below.

Substrate	$g\ (mm)$	ϵ_r	$f'\ (GHz)$
Rogers RT/duriod 6002	$0.218\ mm$	2.94	$12.7\ GHz$
FR4-epoxy	$0.244\ mm$	4.4	$12.4\ GHz$
Rogers RT/duriod 6006	$0.275\ mm$	6.15	$12.2\ GHz$

Table 5.1: Summary of simulations of hybrid waveguides with different substrate materials.

Hence, it was found that the prediction that the upper cutoff frequency, f' decreases with increasing dielectric constant, ϵ_r is consistent with the simulation results.

5.3 Varying Groove Depth

The relationship in Equation 5.8 suggests that as the groove depth, h of the corrugated metallic strip increases, the upper cutoff frequency, f' decreases and the bandwidth decreases.

The following graph of dispersion relations shows the dispersion curves of the SSPPs on corrugated metallic strips with different groove depths, h of 4.0 mm, 3.5 mm and 3.0 mm. The group velocity, v_g of the SSPPs is represented by the gradient of a dispersion curve, and the cutoff frequency, f' is the frequency at which the gradient of the curve is zero. It is observed from Figure 5.4 that as the groove depth, h increases, the cutoff frequency, f' occurs at a lower frequency.

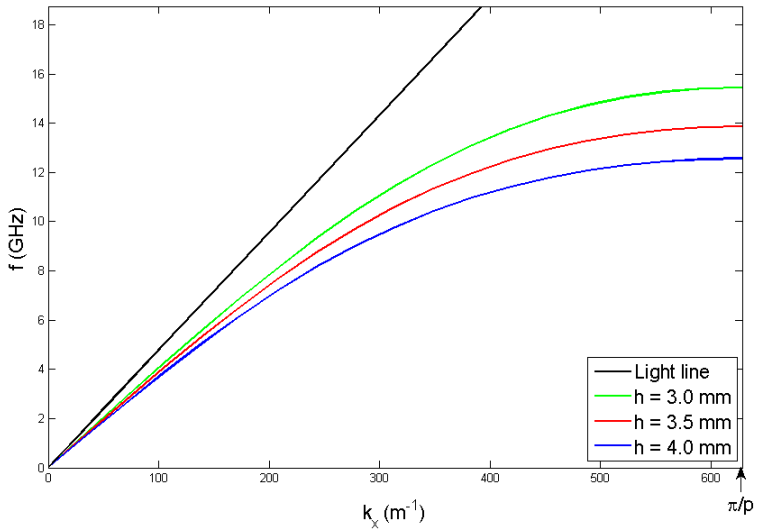

Figure 5.4: Light line and dispersion relations of SSPPs on hybrid waveguides with different groove depths, h.

Further verification of such a relationship was carried out by simulating the $S11$ and $S21$ parameters of the hybrid waveguides with different groove depth, h. The following graphs in Figure 5.5, 5.6 and 5.7 are the S parameters of the hybrid waveguides with $h = 3.0\ mm$, $h = 3.5\ mm$ and $h = 4.0\ mm$ respectively.

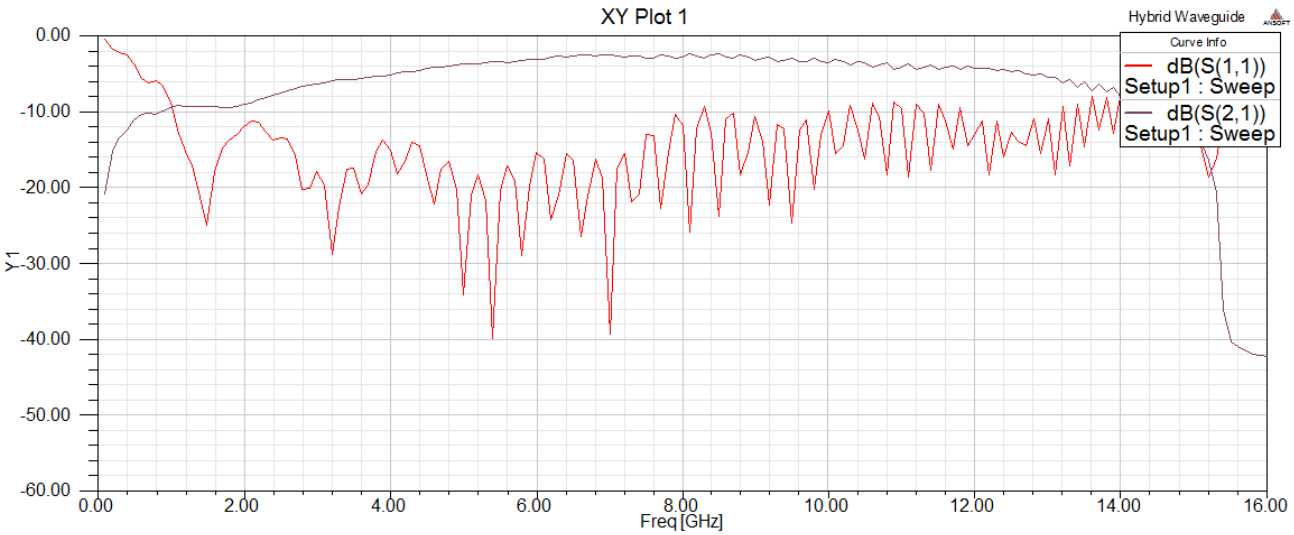

Figure 5.5: S parameters of the hybrid waveguide with a groove depth of $h = 3.0\ mm$.

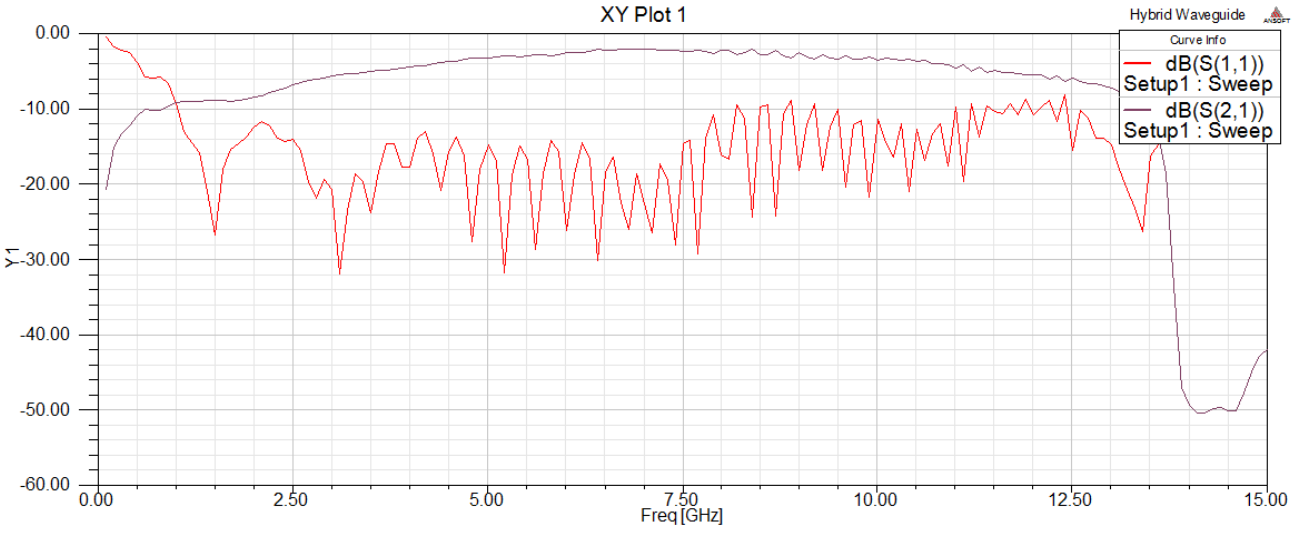

Figure 5.6: S parameters of the hybrid waveguide with a groove depth of $h = 3.5\ mm$.

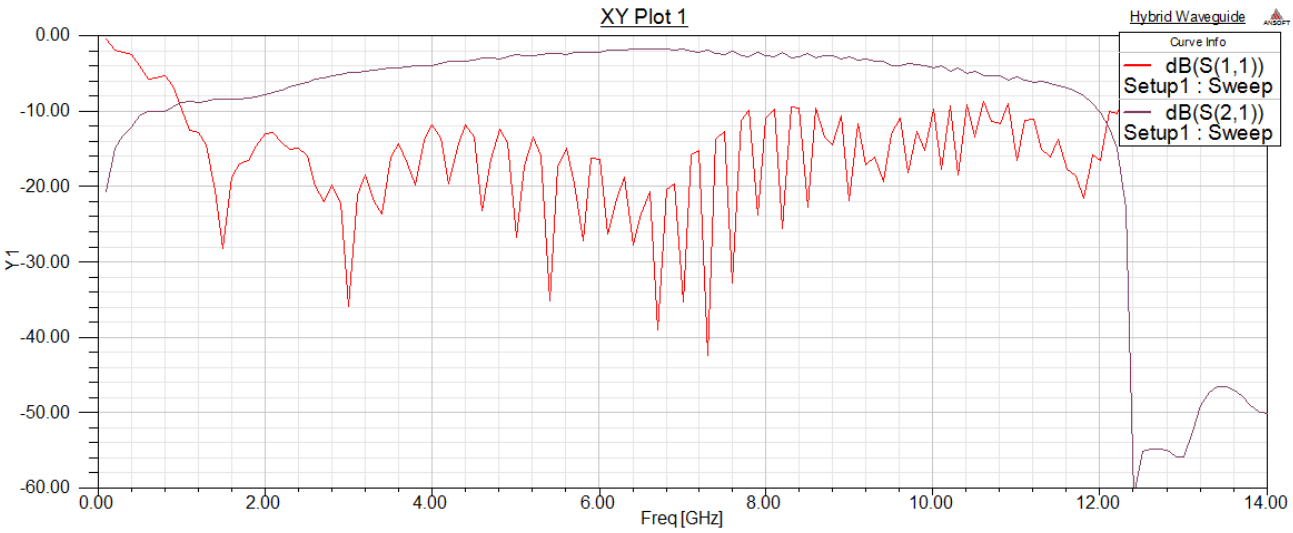

Figure 5.7: S parameters of the hybrid waveguide with a groove depth of $h = 4.0\ mm$.

Choosing the cutoff frequency, f' to be first frequency at which the $S21$ parameter is lower than $-25\ dB$ in the vicinity of a large drop of the $S21$ parameter, the results are summarized in Table 5.2 below.

Substrate	ϵ_r	$h\ (mm)$	$f'\ (GHz)$
FR4-epoxy	4.4	3.0	15.4 GHz
FR4-epoxy	4.4	3.5	13.8 GHz
FR4-epoxy	4.4	4.0	12.4 GHz

Table 5.2: Summary of simulations of hybrid waveguides with different groove depths, h.

The simulation results agree with the prediction that the cutoff frequencies, f' decreases with increasing groove depth, h. Therefore, despite the differences in the actual corrugated metallic strip in the hybrid waveguide and the infinitely thick corrugated metal used to provide the analytic solutions, Equations 4.9 and 5.8 do provide useful insights into the behaviour of SSPPs on the hybrid waveguide.

Chapter 6

Ring Resonators on the Hybrid Waveguides

Ring resonators in optical dielectric waveguides had already been studied as early as in the year 1969 [14]. A ring resonator often takes the form of a circular or racetrack-shaped waveguide, positioned adjacent to one or more straight waveguides known as buses. A fraction of the energies in a bus would be coupled into the ring resonator, which selectively allows only certain frequencies to pass through the bus. Hence, ring resonators on buses function as filters in a network.

Ring resonators in optical frequencies have found many uses in switching and modulation [20]. In addition, ring resonators can also be used in lasers [9] and sensors [8] due to its ability of frequency selection. Recently, ring resonators in plasmonic waveguides have also been studied, such as the propagation of SSPs in an array of silver nanorods [26] and propagation of SSPPs in domino ring resonators [12]. This chapter demonstrates the results of the incorporation of ring resonators in the hybrid waveguides.

6.1 Modeling the Ring Resonator

A single bus ring resonator, as shown in Figure 6.1, is one of the simplest configurations of ring resonators. The radius of the ring resonator is given by R and the coupling region is denoted by the rectangle with red dotted outline.

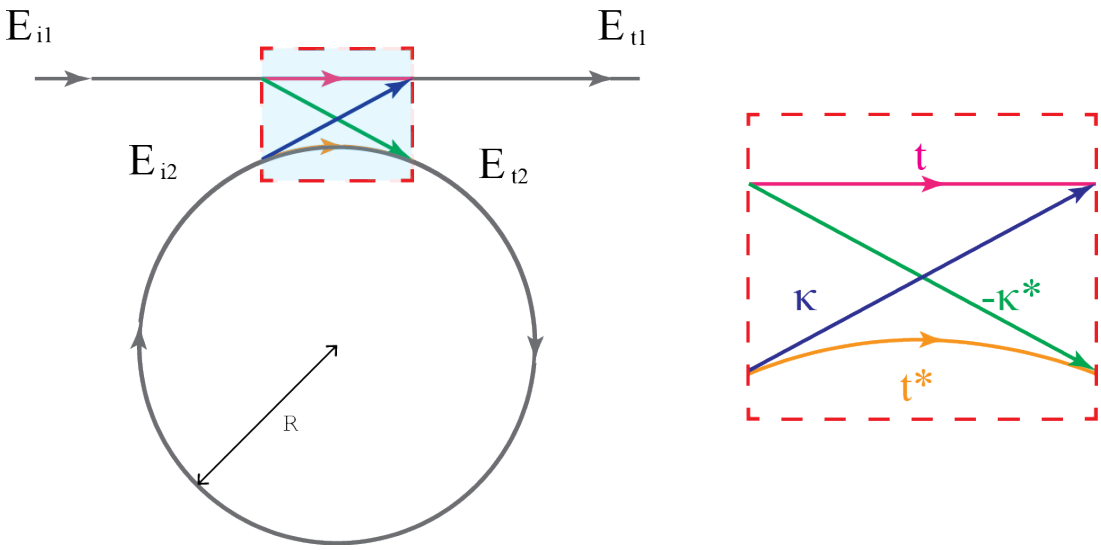

Figure 6.1: The configuration of a single bus ring resonator.

For the case in which waves are travelling in a single direction along the bus and that the total energies of the waves entering and leaving the couplng region are the same, the interaction in the coupling region is given by the following matrix relation [28].

$$\begin{pmatrix} E_{t1} \\ E_{t2} \end{pmatrix} = \begin{pmatrix} t & \kappa \\ -\kappa^* & t^* \end{pmatrix} \begin{pmatrix} E_{i1} \\ E_{i2} \end{pmatrix} \tag{6.1}$$

where E_{i1}, E_{i2}, E_{t1} and E_{t2} are the electric field strengths at the positions as labeled in Figure 6.1, κ is related to the coupling of waves from the bus to the ring and vice versa, whereas t describes the transmission along the bus or the ring resonator in the coupling region. t can be further written as

$$t = |t|e^{i\phi_t} \tag{6.2}$$

where $|t|$ is the coupling loss and ϕ_t is the phase of the coupler [19].

Arising from the reciprocity of the configuration, the coupling matrix in Equation 6.1 is unitary [28], implying that

$$|t|^2 + |\kappa|^2 = 1 \tag{6.3}$$

Without loss of generality, the input electric field, E_{i1} is set to unity so as to simplify the analysis.

The value of E_{i2} is given by

$$E_{i2} = \alpha e^{i\theta} E_{t2} \tag{6.4}$$

where α is the loss per circulation with $\alpha = 1$ representing no loss, and θ is the phase shift round the ring resonator [19].

From Equations 6.1, 6.2 and 6.4, we have

$$E_{t1} = \frac{-\alpha + te^{-i\theta}}{-\alpha t^* + e^{-i\theta}} \tag{6.5}$$

$$E_{i2} = \frac{-\alpha\kappa^*}{-\alpha t^* + e^{-i\theta}} \tag{6.6}$$

$$E_{t2} = \frac{-\kappa^*}{1 - \alpha t^* e^{i\theta}} \tag{6.7}$$

The normalized power output, P_{t1} on the bus is therefore

$$P_{t1} = |E_{t1}|^2 = \frac{\alpha^2 + |t|^2 - 2\alpha|t|\cos(\theta + \phi_t)}{1 + \alpha^2|t|^2 - 2\alpha|t|\cos(\theta + \phi_t)} \tag{6.8}$$

Hence, the value of the power output, P_{t1} is a periodic function of the phase shift of the waves round the ring resonator, θ.

The dependence of the output power, P_{t1} on the frequency, f of the waves lies in the the influence of the frequency, f on the phase shift, θ round the ring resonator as follows.

$$\theta = \frac{2\pi R n_{eff}}{\lambda_0} \tag{6.9}$$

$$= \frac{2\pi R n_{eff} f}{c} \tag{6.10}$$

where λ_0 is the free space wavelength of the waves and n_{eff} is the effective refractive index of the waveguide.

In the case of the hybrid waveguide, the effective refractive index, n_{eff} experienced by the SSPPs could be expressed as the ratio of the wavenumber of the SSPPs on the hybrid waveguide, k_x which is approximated as in Equation 4.10, to the wavenumber of the guided waves, k_0.

$$n_{eff} = \frac{k_x}{k_0} \tag{6.11}$$

$$= \frac{k_0\sqrt{1+\left(\frac{a}{p}\right)^2 \tan^2\left(h\frac{\omega}{c}\right)}}{k_0} \tag{6.12}$$

$$= \sqrt{1+\left(\frac{a}{p}\right)^2 \tan^2\left(h\frac{\omega}{c}\right)} \tag{6.13}$$

$$= \sqrt{1+\left(\frac{a}{p}\right)^2 \tan^2\left(h\frac{2\pi f}{c}\right)} \tag{6.14}$$

From Equation 6.8, Equation 6.10 and Equation 6.14, we then have

$$P_{t1} = \frac{\alpha^2 + |t|^2 - 2\alpha|t|\cos\left(\frac{2\pi Rf}{c}\sqrt{1+\left(\frac{a}{p}\right)^2 \tan^2\left(h\frac{2\pi f}{c}\right)} + \phi_t\right)}{1+\alpha^2|t|^2 - 2\alpha|t|\cos\left(\frac{2\pi Rf}{c}\sqrt{1+\left(\frac{a}{p}\right)^2 \tan^2\left(h\frac{2\pi f}{c}\right)} + \phi_t\right)} \tag{6.15}$$

The plot of power output, P_{t1} against the frequency, f with α and $|t|$ arbitrarily set as 0.70 and 0.75, is as follows.

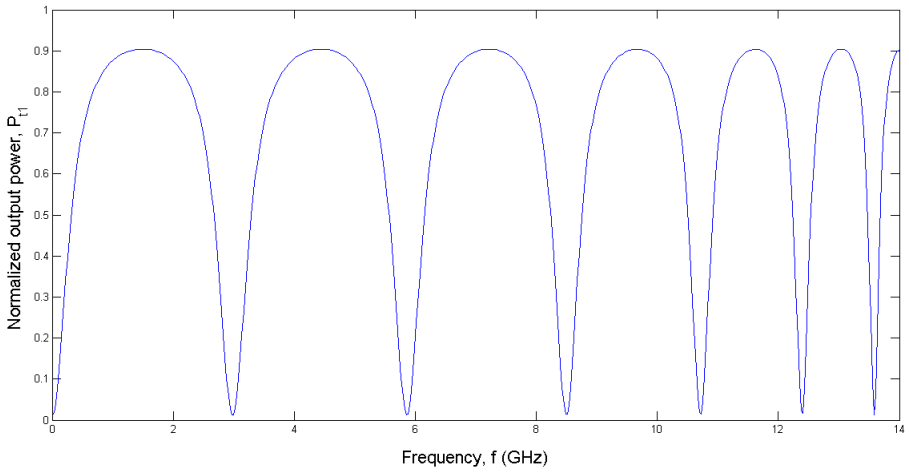

Figure 6.2: The graph of P_{t1} against f.

It is shown that instead of allowing signals of the entire band of frequencies to pass, the ring resonator hinders the passage of signals of some frequencies. As aforementioned and shown, ring resonators are often used as filters in a network.

6.2 Simulation Results

With the ring resonators incorporated to the hybrid waveguide as shown in Figure 6.3 where two ring resonators with outer radii of 15.92 mm and inner radii of 10.92 mm were placed adjecent to the straight corrugated strip.

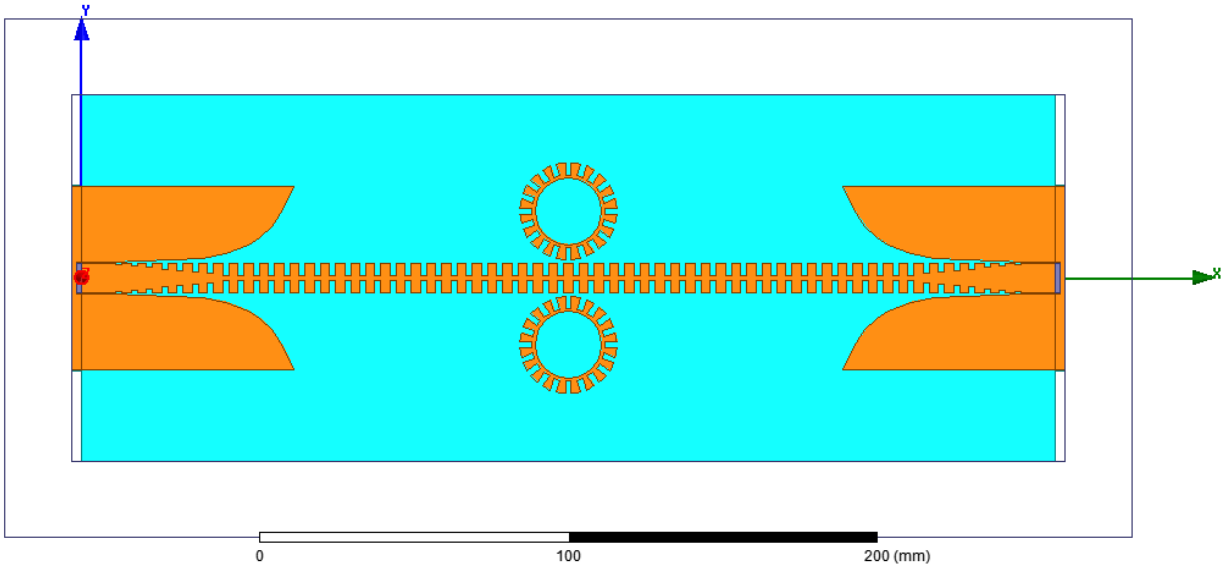

Figure 6.3: The hybrid waveguide with ring resonators.

The $S21$ parameter of the hybrid waveguide were then obtained from the simulation. It is observed the addition of ring resonators changes the graph of the $S21$, a measure of the transmitted power output of the hybrid waveguide, from the response in Figure 6.4 to the one in Figure 6.5, resembles the the graph in Figure 6.2 to some extent.

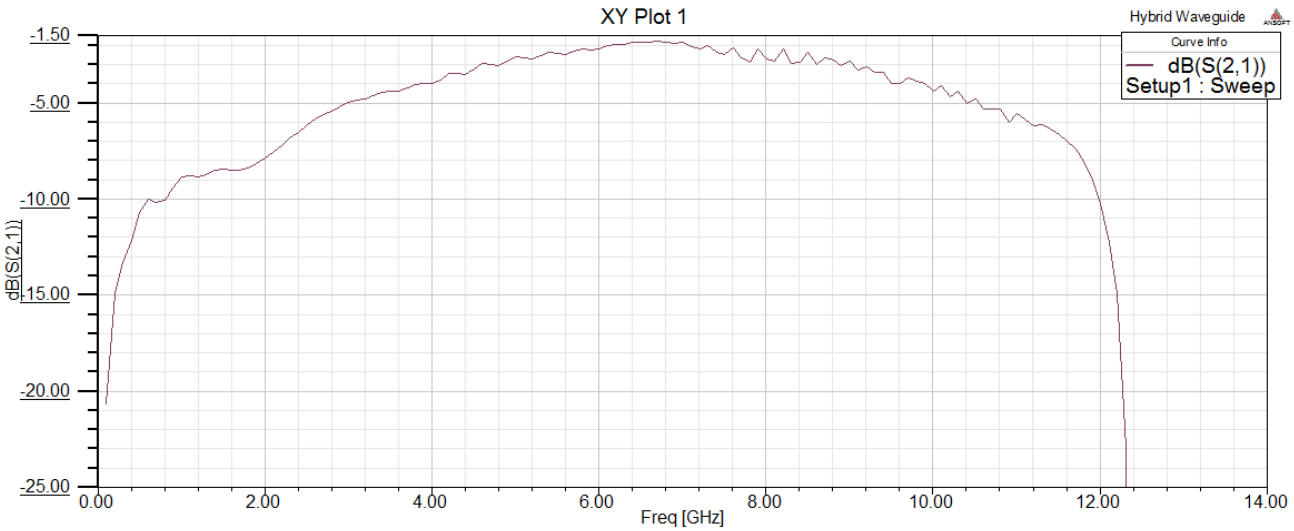

Figure 6.4: $S21$ parameters of the hybrid waveguide without ring resonators.

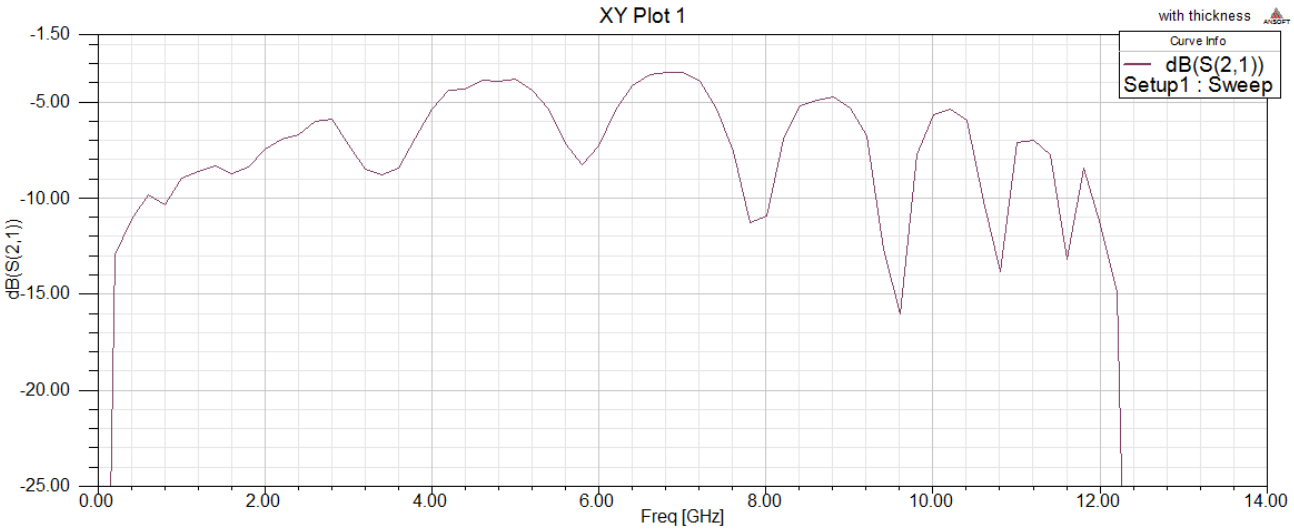

Figure 6.5: $S21$ parameters of the hybrid waveguide with ring resonators.

As seen in Figure 6.5, the $S21$ parameter is high at certain frequencies such as 6.8 GHz, 8.8 GHz and 10.2 GHz but low frequencies such as 7.8 GHz, 9.6 GHz and 10.8 GHz. The plots of the magnitude of the electric field are given in Figures 6.6, 6.7, 6.8, 6.9, 6.10 and 6.11 respectively.

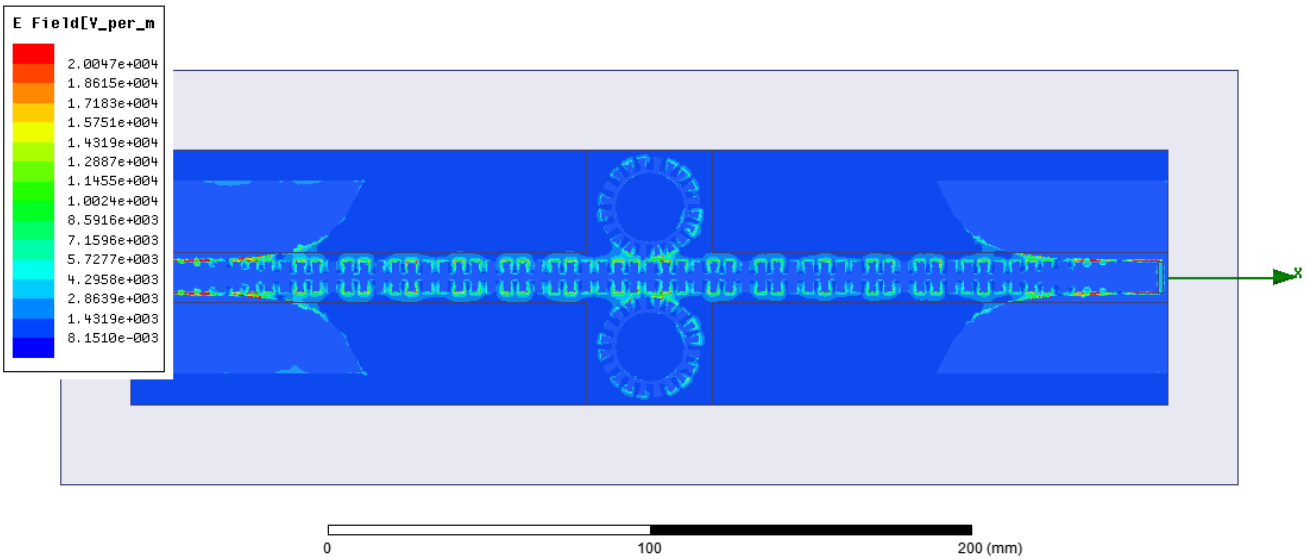

Figure 6.6: The plot of electric field magnitude at 6.8 GHz.

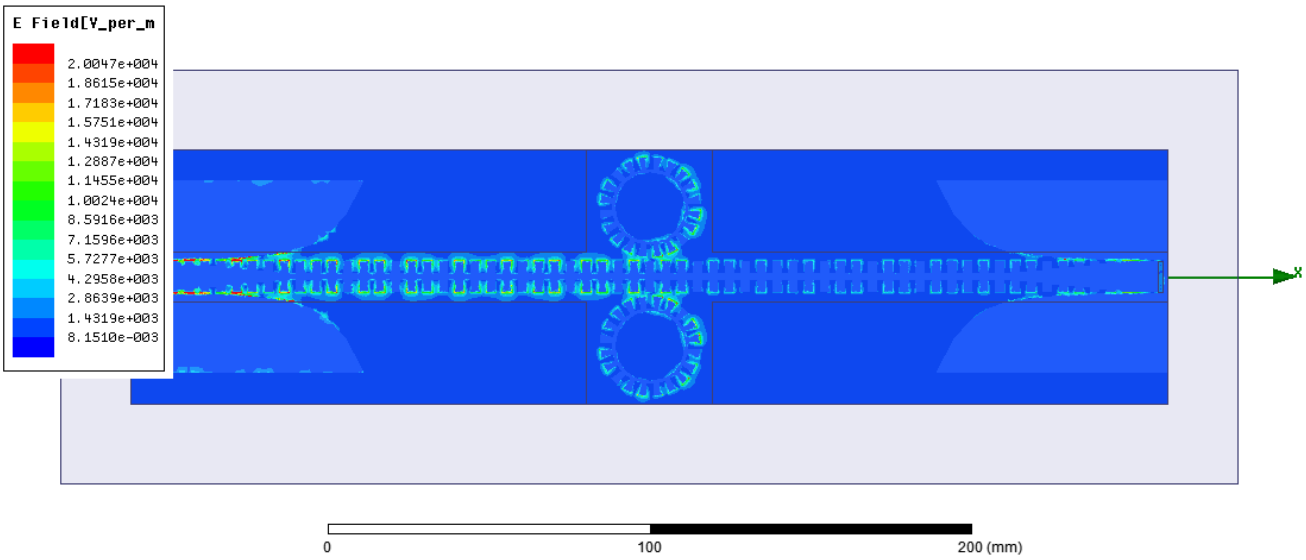

Figure 6.7: The plot of electric field magnitude at 7.8 GHz.

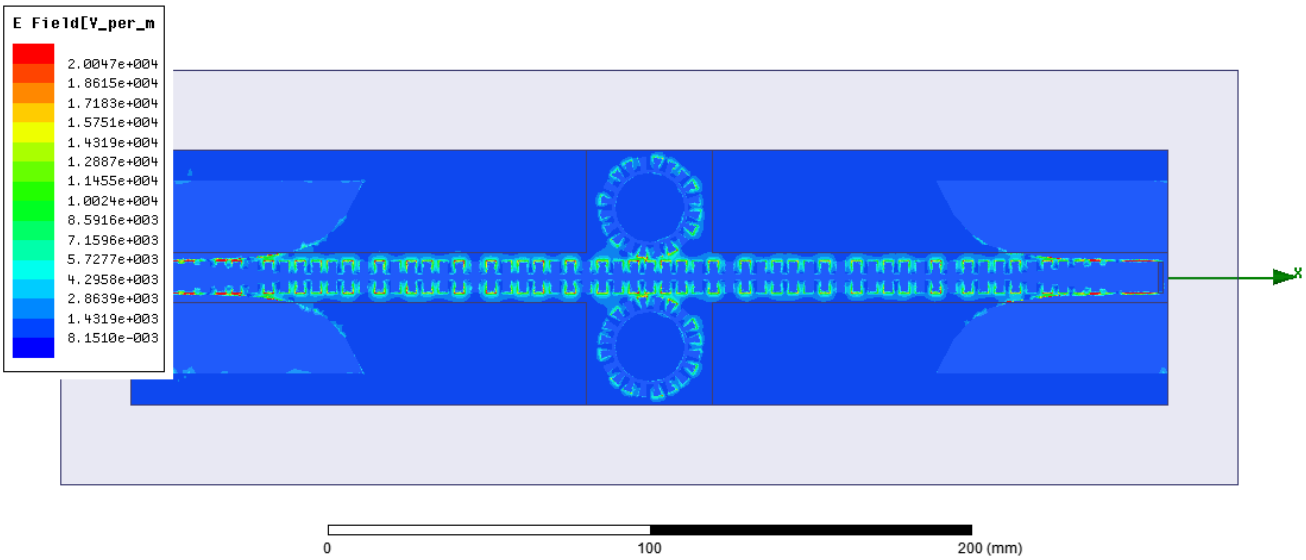

Figure 6.8: The plot of electric field magnitude at 8.8 GHz.

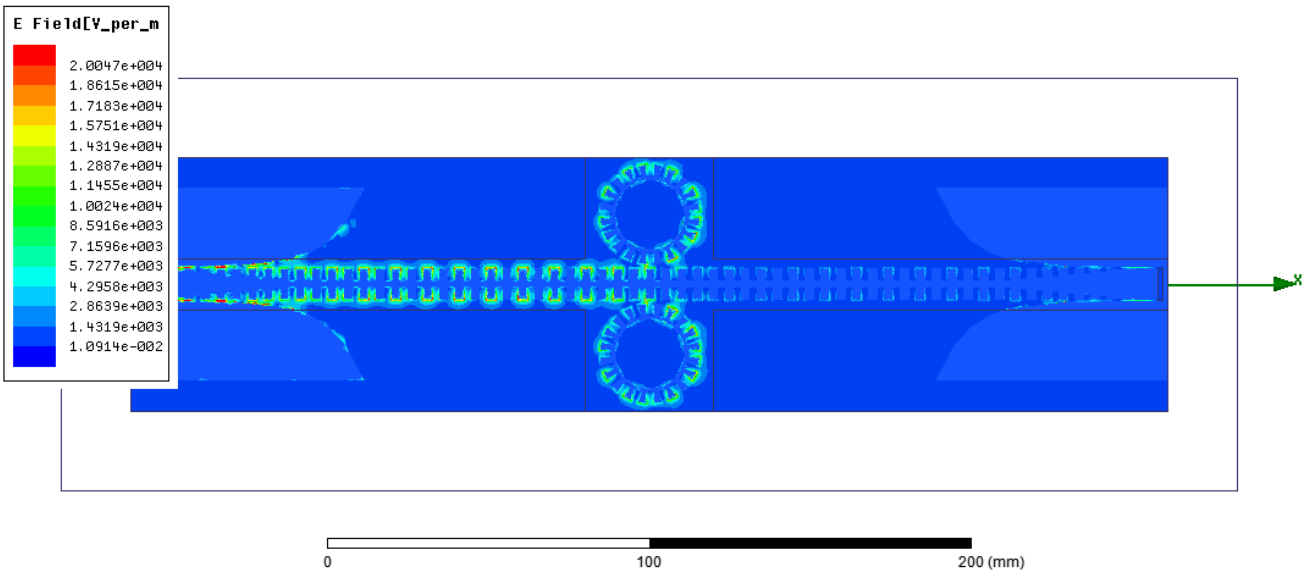

Figure 6.9: The plot of electric field magnitude at 9.6 GHz.

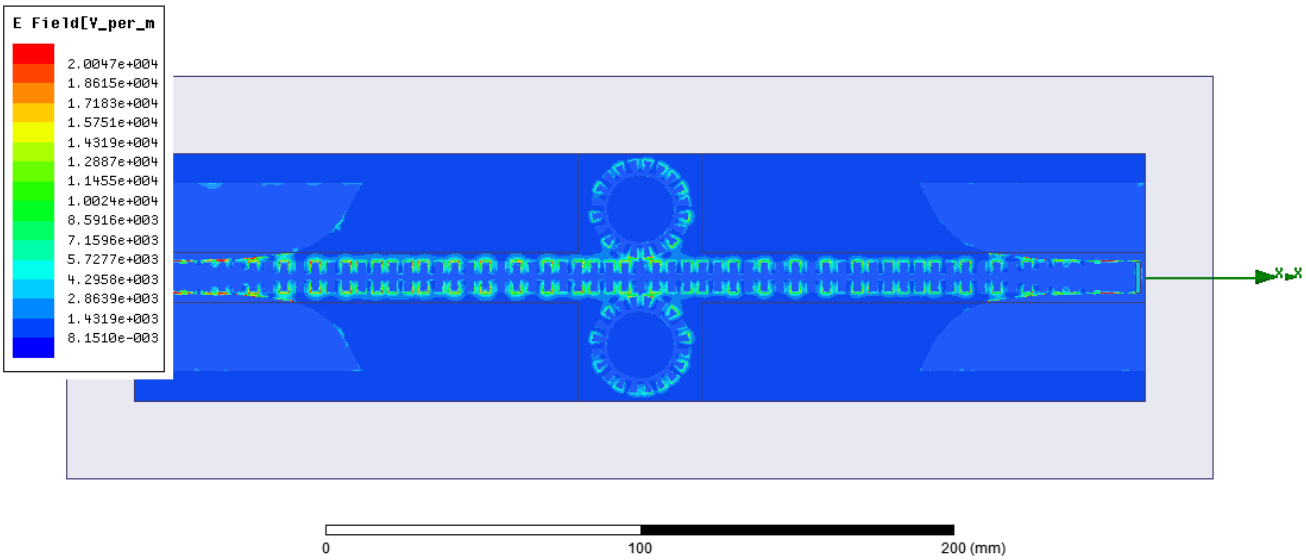

Figure 6.10: The plot of electric field magnitude at 10.2 GHz.

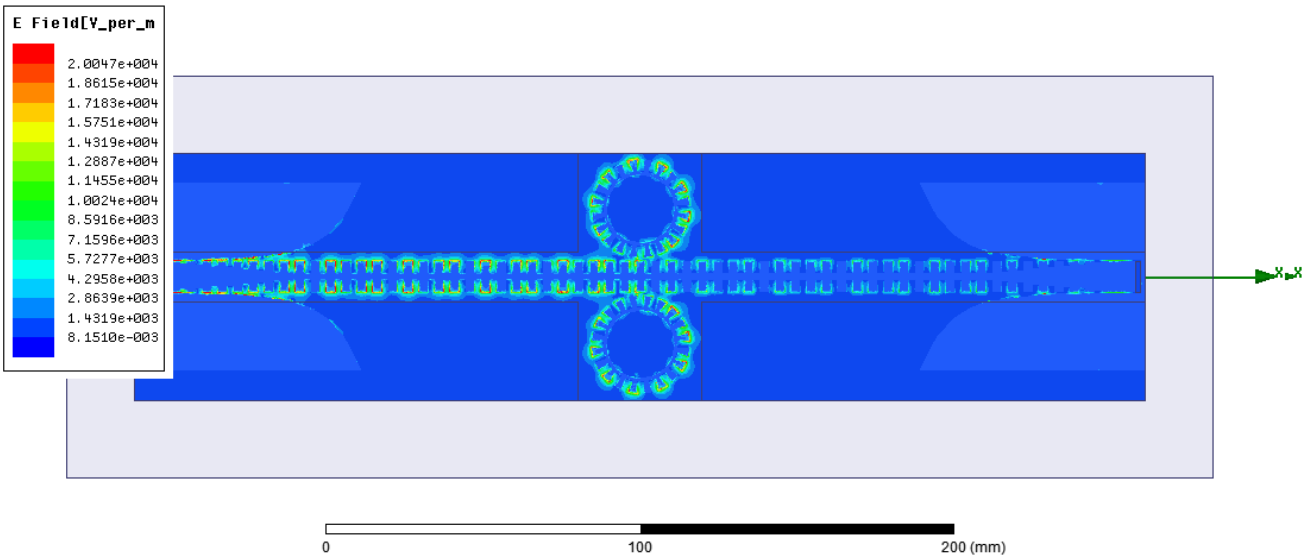

Figure 6.11: The plot of electric field magnitude at 10.8 GHz.

The simulation results confirms that the hybrid waveguide with ring resonators allows some frequencies to pass but not the others, acting as a filter that prohibits the transmission of signals of certain frequencies at some intervals. A filter of this kind is similar to a notch type filter, a bandstop filter with narrow stopbands [19]. However, it is noted that some fraction of energies do reach the

output port even at the frequencies at which the signals are supposed to be prohibited. This might arise from the inefficient coupling of energy from the straight waveguide to the ring resonators. This problem however will not be discussed as it is beyond the scope of the project.

In summary, the incorporation of ring resonators to the hybrid waveguide changes the bandpass characteristics of the waveguide to a response with several stopbands, whose interval can be altered by changing the radius of the ring and thus the phase shift round the ring at a given frequency.

Chapter 7

Conclusion and Future Work

7.1 Concluding Remarks

The verification of the conversion of guided waves in a conventional CPW to SSPPs in a plasmonic metamaterial waveguide and vice versa confirms the possibility of convenient transformation of signals which might take several forms during the course of their transmission from a source to the destination. The feasibility of such a conversion is undoubtedly a key to lowering the barrier of greater integration of SSPPs to the conventional microwave circuitry.

On top of that, the demonstration of the manipulation of SSPPs on the hybrid waveguide by means of varying the physical parameters of the hybrid waveguide implies that SSPPs could be highly controllable. As a result, the bandwidth of SSPPs on the hybrid waveguide could be easily adapted to fulfill the requirement in a network.

In addition, the incorporation of ring resonators in the hybrid waveguide was shown to successfully alter the spectral response from the bandpass response to the one with stopbands at some intervals. Since different configurations of ring resonators give rise to different spectral characteristics, there lies huge potential in the functionality and the versatility of the hybrid waveguide to accommodate to different niches and applications, hence suggesting promising prospects of SSPPs on a hybrid waveguide.

7.2 Future Work

Experiments can be conducted for further verification of the conversion of guided waves to SSPPs and vice versa on a hybrid waveguide as well as the effects of varying physical parameters and incorporation of ring resonators on the hybrid waveguide. The hybrid waveguide could be fabricated with a printed circuit board (PCB) whereas the S parameters could be measured using a vector network analyzer (VNA). On top of that, the plot of the electric field strength over the hybrid waveguide can also be carried out using a home made two-dimensional field mapping system [30] to measure the electric field strength in the z direction over the hybrid waveguide as shown in Figure 7.1.

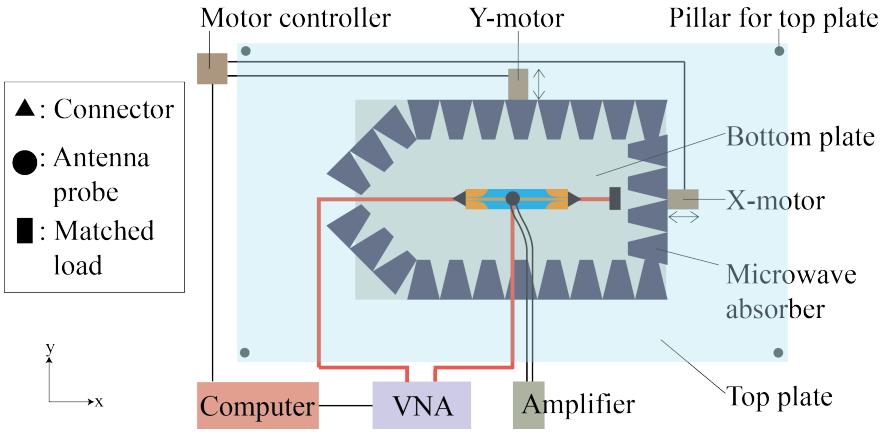

Figure 7.1: A homemade 2D field mapping system.

Having demonstrated the conversion between guided waves and SSPPs on the hybrid waveguide, the next concern might be achieving higher efficiency in terms of lower loss of the hybrid waveguide. While there seems to have no obvious analytic solution to the issue, computational methods could be used instead. One possible option to improve the performance of the hybrid waveguide is using topology optimization, a design approach that optimizes the distribution of material within a design domain such that the value of the objective function in the output domain, subject to some predetermined constraints, is maximized or minimized. Topology optimization is often accompanied by finite element analysis (FEA) in its implementation. This method has in fact been used for the excitations of SPPs in optical frequencies [3]. In the case of the hybrid waveguide, the design domain, Ω_{des} and the output domain, Ω_{out} could be defined as in Figure 7.2.

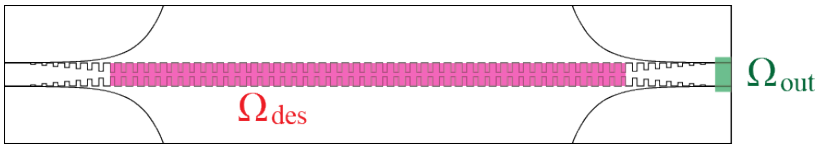

Figure 7.2: Design domain, Ω_{des} (shaded in red) and output domain, Ω_{out} (shaded in green) in topology optimization of the hybrid waveguide.

The optimization problem could be written as

$$\max_{\vec{\rho}} \sum_{i} \int_{\Omega_{out}} |E(f_i)|^2 \, d\Omega_{out} \tag{7.1}$$

where $\vec{\rho}$ is the density distribution vector of the densities of the finite elements whereas f_i is an element of the desired set of frequencies. The formulation above is a maximization of the power in the output domain, Ω_{out} by varying the layout of the material, PEC in this case, in the design domain, Ω_{des}, thus achieving a maximized amount of power reaching the output port of the waveguide.

There are of course other directions to which future research could be steered. However, a thorough understanding of SSPPs on plasmonic metamaterial must first be established. It is hoped that this project, which examines the SSPPs on a hybrid waveguide, could help to provide some useful insights into SSPPs on a plasmonic metamatetrial as well as to lay a better foundation for the theoretical researches, computational simulations and experimental investigations in the future.

Bibliography

[1] Nobel Media AB, *The 2009 nbel prize in physics - press release*, 2009.

[2] CST Computer Simulation Technology AG, *Microwave & rf components*, 2015.

[3] Jacob Andkjær, Shinji Nishiwaki, Tsuyoshi Nomura, and Ole Sigmund, *Topology optimization of grating couplers for the efficient excitation of surface plasmons*, Journal of the Optical Society of America B **27** (2010), no. 9, 1828 (English).

[4] *An introduction to hfss: Fundamental principles, concepts, and use*, Ansoft, LLC, Pittsburgh, PA.

[5] Harry A. Atwater, *The promise of plasmonics*, Vol. 296, 2007 (English).

[6] K. C. Gupta, *Microstrip lines and slotlines*, Artech House, Boston, 1996 (English).

[7] Charles Kittel, *Introduction to solid state physics*, Wiley, Hoboken, NJ, 2005 (English).

[8] A. Ksendzov and Y. Lin, *Integrated optics ring-resonator sensors for protein detection*, Opt. Lett. **30** (2005Dec), no. 24, 3344–3346.

[9] Bin Liu, Ali Shakouri, and J.E. Bowers, *Wide tunable double ring resonator coupled lasers*, Photonics Technology Letters, IEEE **14** (2002May), no. 5, 600–602.

[10] Matthew J. Lockyear, Alastair P. Hibbins, and J. R. Sambles, *Microwave surface-plasmon-like modes on thin metamaterials*, Physical Review Letters **102** (2009), no. 7, 073901 (English).

[11] Hui F. Ma, Xiaopeng Shen, Qiang Cheng, Wei X. Jiang, and Tie J. Cui, *Broadband and high-efficiency conversion from guided waves to spoof surface plasmon polaritons*, Laser & Photonics Reviews **8** (2014), no. 1, 146–151 (English).

[12] Y. G. Ma, L. Lan, S. M. Zhong, and C. K. Ong, *Experimental demonstration of sub-wavelength domino plasmon devices for compact high-frequency circuit*, Opt. Express **19** (2011Oct), no. 22, 21189–21198.

[13] Stefan A. Maier, *Plasmonics: Fundamentals and applications: Fundamentals and applications*, Springer Science + Business Media, 2007 (German).

[14] E. A. J. Marcatili, *Bends in optical dielectric guides*, Bell System Technical Journal **48** (1969), no. 7, 2103–2132.

[15] J. B. Pendry, L. Martín-Moreno, and F. J. Garcia-Vidal, *Mimicking surface plasmons with structured surfaces*, Science **305** (2004), no. 5685, 847–848, available at `http://www.sciencemag.org/content/305/5685/847.full.pdf`.

[16] S Pinon, D L Diedhiou, A-M Gue, N Fabre, G Prigent, V Conedera, E Rius, C Quendo, B Potelon, J-F Favennec, and A Boukabache, *Development of a microsystem based on a microfluidic network to tune and reconfigure rf circuits*, Journal of Micromechanics and Microengineering **22** (2012), no. 7, 074005.

[17] J.R. Powell, *The quantum limit to moore's law*, Proceedings of the IEEE **96** (2008Aug), no. 8, 1247–1248.

[18] David M. Pozar, *Microwave engineering*, John Wiley, Hoboken, NJ, 2004 (English).

[19] D. G. Rabus, *Integrated ring resonators: the compendium*, Vol. 127. Springer, Berlin, 2007 (English).

[20] G. T. Reed, G. Mashanovich, D. J. Thomson, and F. Y. Gardes, *Silicon optical modulators*, Nature Photonics **4** (2010), no. 8, 518–526 (English).

[21] R. H. Ritchie, *Plasma losses by fast electrons in thin films*, Phys. Rev. **106** (1957Jun), 874–881.

[22] Xiaopeng Shen, Tie Jun Cui, Diego Martin-Cano, and Francisco J. Garcia-Vidal, *Conformal surface plasmons propagating on ultrathin and flexible films*, Proceedings of the National Academy of Sciences **110** (2013), no. 1, 40–45, available at `http://www.pnas.org/content/110/1/40.full.pdf+html`.

[23] Rainee Simons, *Coplanar waveguide circuits, components, and systems*, John Wiley, New York, 2001 (English).

[24] Kyungjun Song and P. Mazumder, *Active terahertz spoof surface plasmon polariton switch comprising the perfect conductor metamaterial*, Electron Devices, IEEE Transactions on **56** (2009Nov), no. 11, 2792–2799.

[25] Volker J. Sorger, Rupert F. Oulton, Ren-Min Ma, and Xiang Zhang, *Toward integrated plasmonic circuits*, MRS Bulletin **37** (20128), 728–738.

[26] Nahid Talebi, Ata Mahjoubfar, and Mahmoud Shahabadi, *Plasmonic ring resonator*, Journal of the Optical Society of America B **25** (2008), no. 12, 2116–2122 (English).

[27] Masayoshi Tonouchi, *Cutting-edge terahertz technology*, Nature Photonics **1** (2007), no. 2, 97–105 (English).

[28] A. Yariv, *Universal relations for coupling of optical power between microresonators and dielectric waveguides*, Electronics Letters **36** (2000), no. 4, 321 (English).

[29] Anatoly V. Zayats, Igor I. Smolyaninov, and Alexei A. Maradudin, *Nano-optics of surface plasmon polaritons*, Physics Reports **408** (2005), no. 3–4, 131 –314.

[30] L. Zhao, X. Chen, and C. K. Ong, *Visual observation and quantitative measurement of the microwave absorbing effect at x band*, Review of Scientific Instruments **79** (2008), no. 12, 124701–124701–5 (English).

Appendix A

Calculating the Characteristic Impedance of a CPW

```
%%%%%%%%%%%%%%%%%%%%%%%%%%%%%%%%%%%%%%%%%%%%%%%%%%%%%%%%%%%%%%%%%%%%%%%%%%%%
% This is a code written for the calculation of the characteristic %
% impedance of a coplanar waveguide (CPW) in the hybrid waveguide. %
%%%%%%%%%%%%%%%%%%%%%%%%%%%%%%%%%%%%%%%%%%%%%%%%%%%%%%%%%%%%%%%%%%%%%%%%%%%%

function Z=CharImp(e,h,t,S,W)

% e = dielectric constant of substrate
% h = groove depth of corrugated strip
% t = thickness of the metal or PEC above the substrate
% S = width of the central strip
%     (refered as 2H in this project)
% W = gap between the central strip and the ground plate
%     (refered as g in this project)

p = 1+log(4*pi*S/t);
q = 1.25*t/pi;
D = p*q;
k0 = S/(S+2*W);
k1 = sinh(pi*S/4/h)/sinh(pi*(S+2*W)/4/h);
k1_t = (S+D)/(S+2*W-D);

ratioK0=ellipke(k0^2)/ellipke(1-k0^2);
ratioK1=ellipke(k1^2)/ellipke(1-k1^2);
ratioK1_t=ellipke(k1_t^2)/ellipke(1-k1_t^2);

% ellipke(m) is a MATLAB function of the complete elliptic integrals of the
% first kind, with m=k^2, where k is the modulus of the complete elliptic
% integrals


eff=1+(e-1)/2*ratioK1*1/ratioK0; % This is the effective dielectric constant without↙
considering the thickness of the metal

eff_t=eff-0.7*t/W*(eff-1)/(ratioK0+0.7*t/W)  % This is the effective dielectric↙
constant with the thickness of metal taken into account

Z=30*pi/sqrt(eff_t)*1/ratioK1_t; % The characteristic impedance when the thickness of↙
the metal taken into account
```